Supplementary Materials for

Large Piezoelectric Response in Chiral Covalent Organic Frameworks via Chirality-Amplified Dipolar Alignment

Xin Liang,[1] Nan Yang,[1] Yang-Yang Wang,[1] Yixin Wang,[1,2] & Qiang Yan[1,2,*]

[1]State Key Laboratory of Molecular Engineering of Polymers, Fudan University, Shanghai 200438, China

[2]Department of Macromolecular Science, Fudan University, Shanghai 200433, China

Table of Contents

S2. Supplementary characterization of crystalline structures and chiral properties of chiral P-COFs and its achiral counterparts.

S3. Supplementary tests on piezoelectric properties of chiral P-COFs and its achiral counterparts.

S4. Theoretical simulation of 3D elastic moduli of chiral P-COFs.

S5. Supplementary tests on piezoelectric effect of chiral P-COF/PDMS composite devices.

S6. Supplementary Tables

S1. Supplementary characterization of chiral cages and chiral P-COFs in chemical structures and properties.

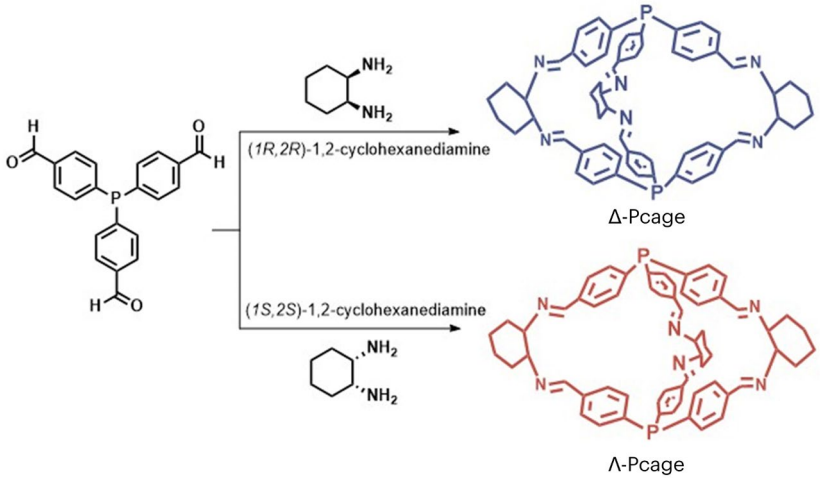

Supplementary Fig. 1 The synthetic procedures of chiral organic cages, Δ- and Λ-Pcage.

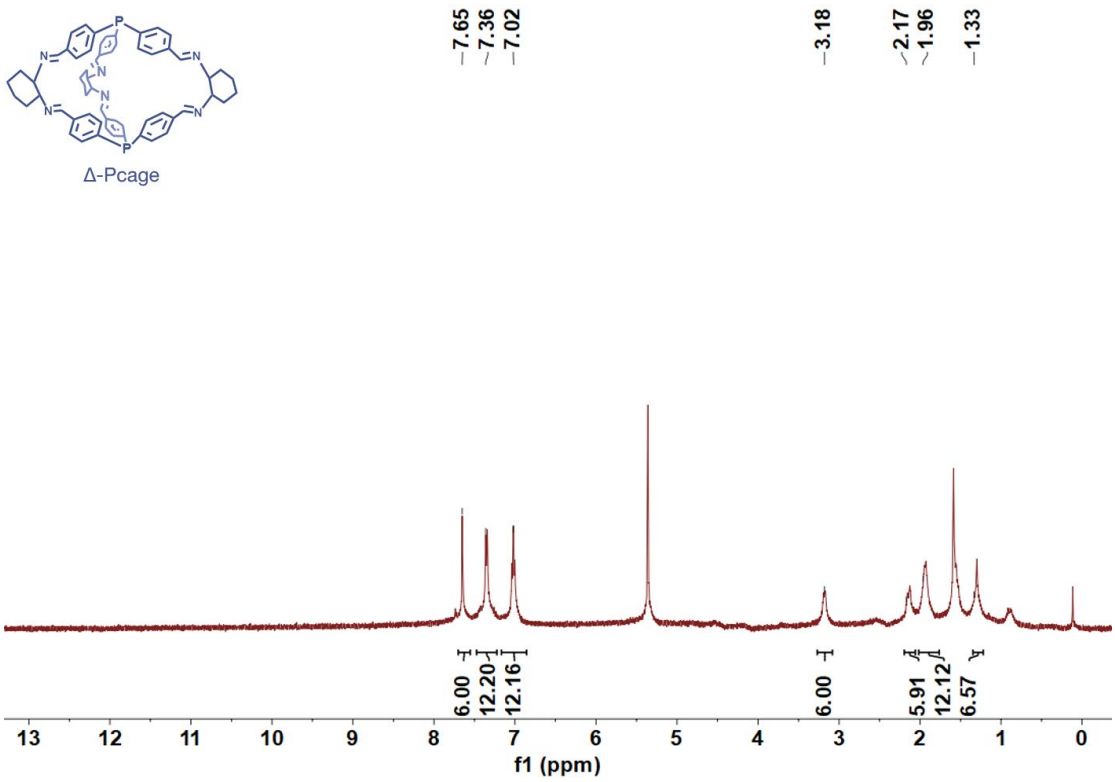

Supplementary Fig. 2 ^{1}H NMR spectra of Δ-Pcage in CD_2Cl_2.

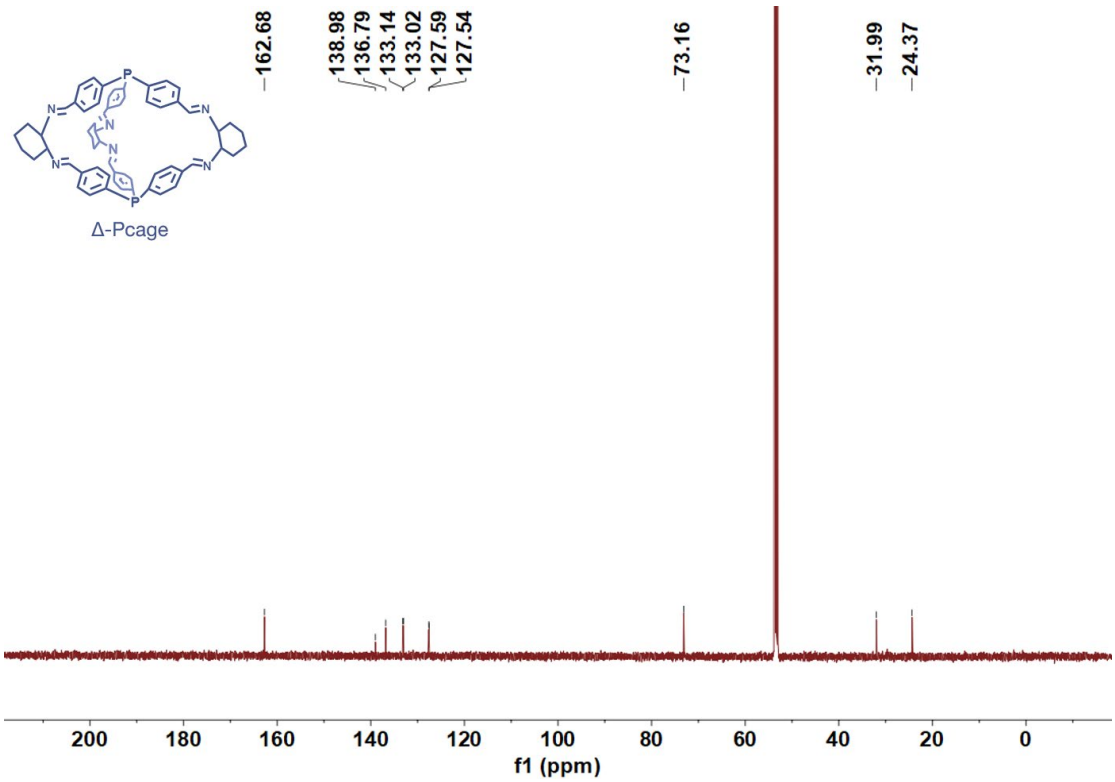

Supplementary Fig. 3 ^{13}C NMR spectra of Δ-Pcage in CD_2Cl_2.

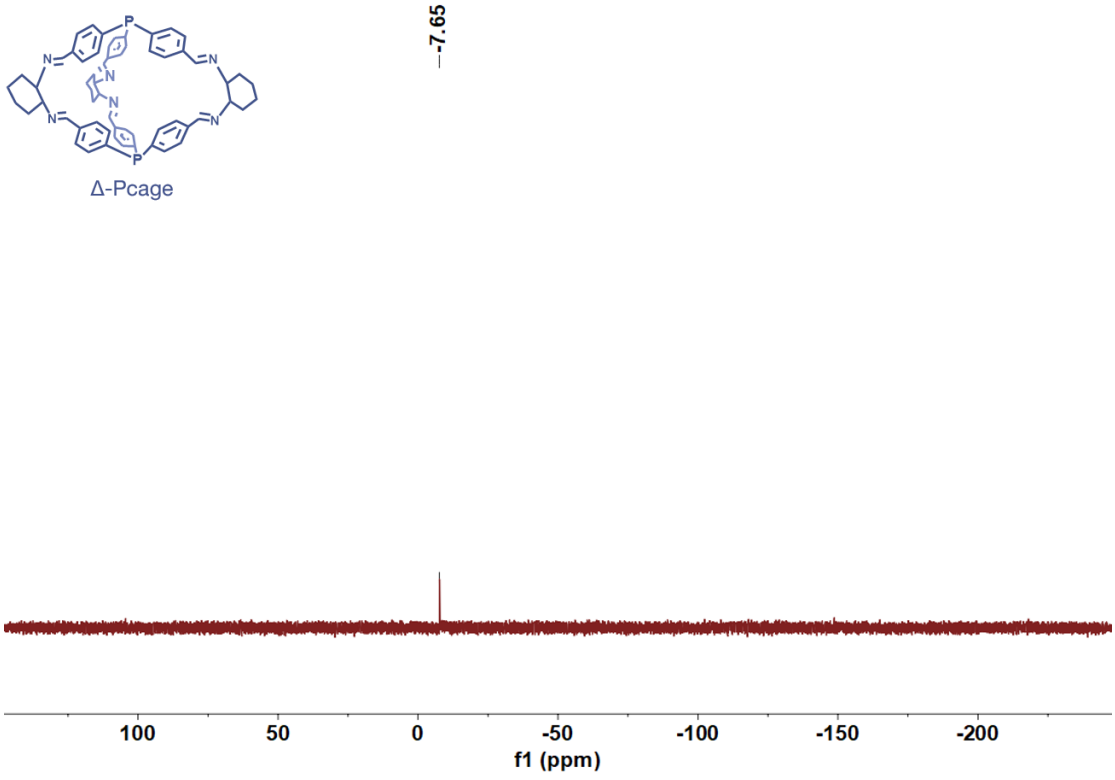

Supplementary Fig. 4 ^{31}P NMR spectra of Δ-Pcage in CD_2Cl_2.

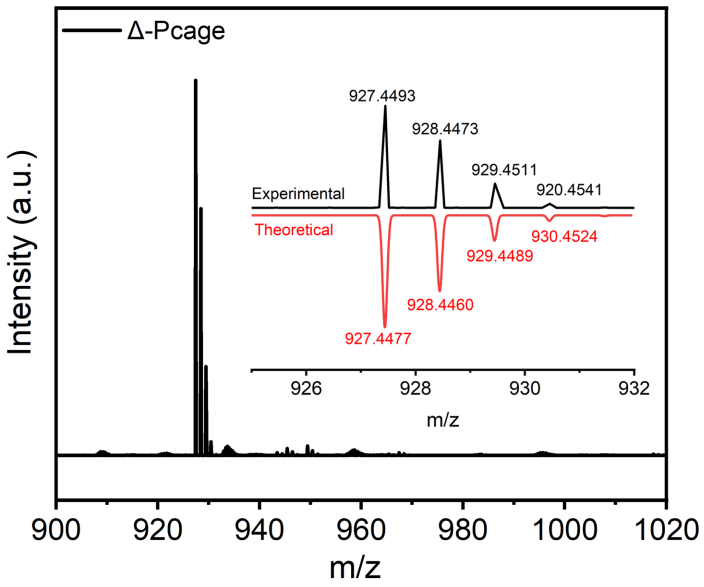

Supplementary Fig. 5 HR-ESI-MS spectrum of Δ-Pcage ($C_{60}H_{60}N_6P_2$, $[M+H]^+$, *m*/*z*, found. 927.4493; calcd. 927.4477).

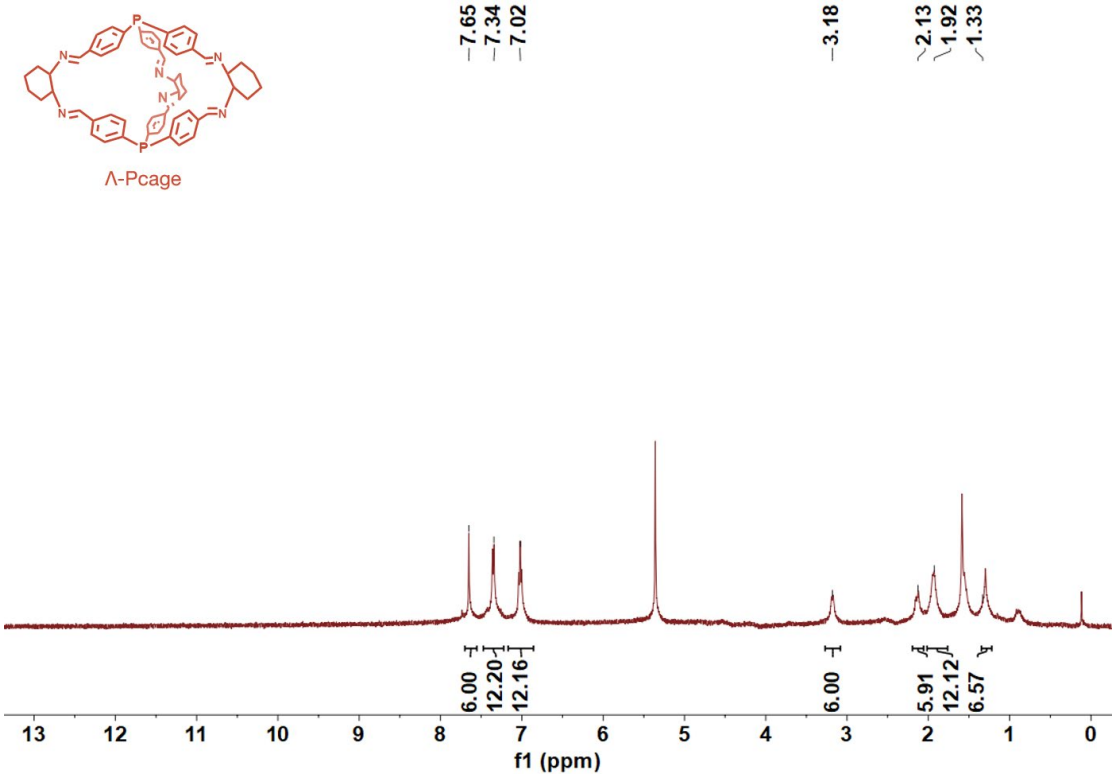

Supplementary Fig. 6 ^{1}H NMR spectra of Λ-Pcage in CD_2Cl_2.

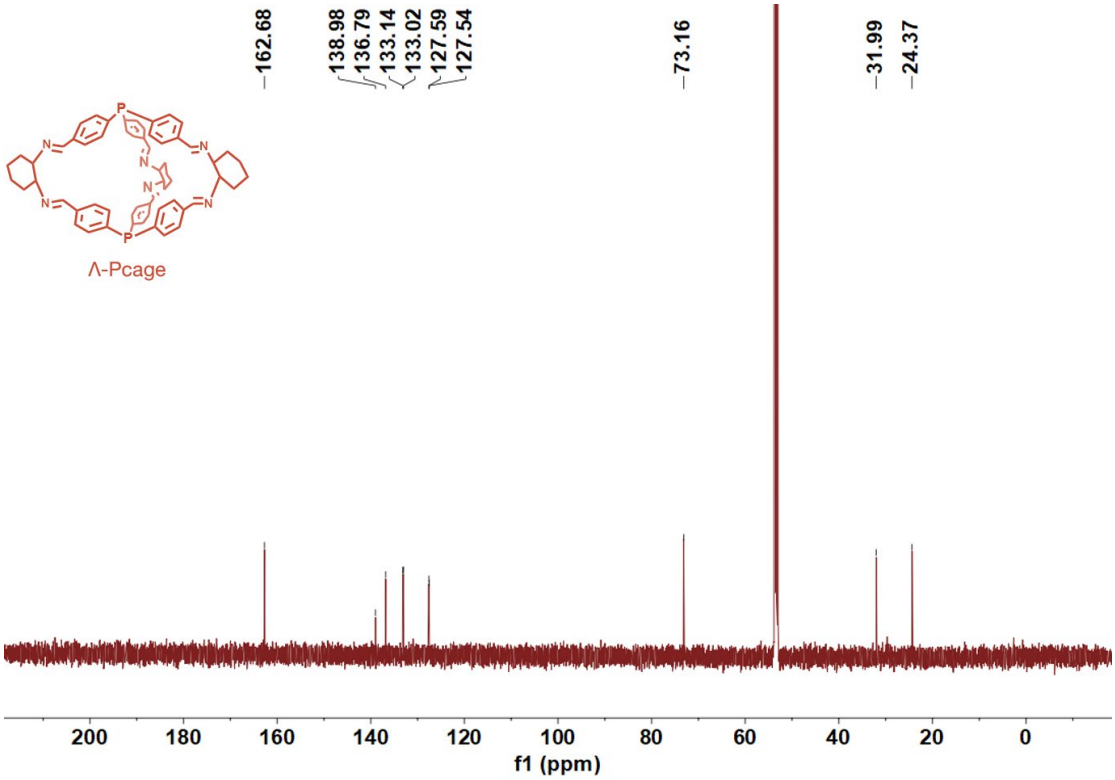

Supplementary Fig. 7 ^{13}C NMR spectra of Λ-Pcage in CD_2Cl_2.

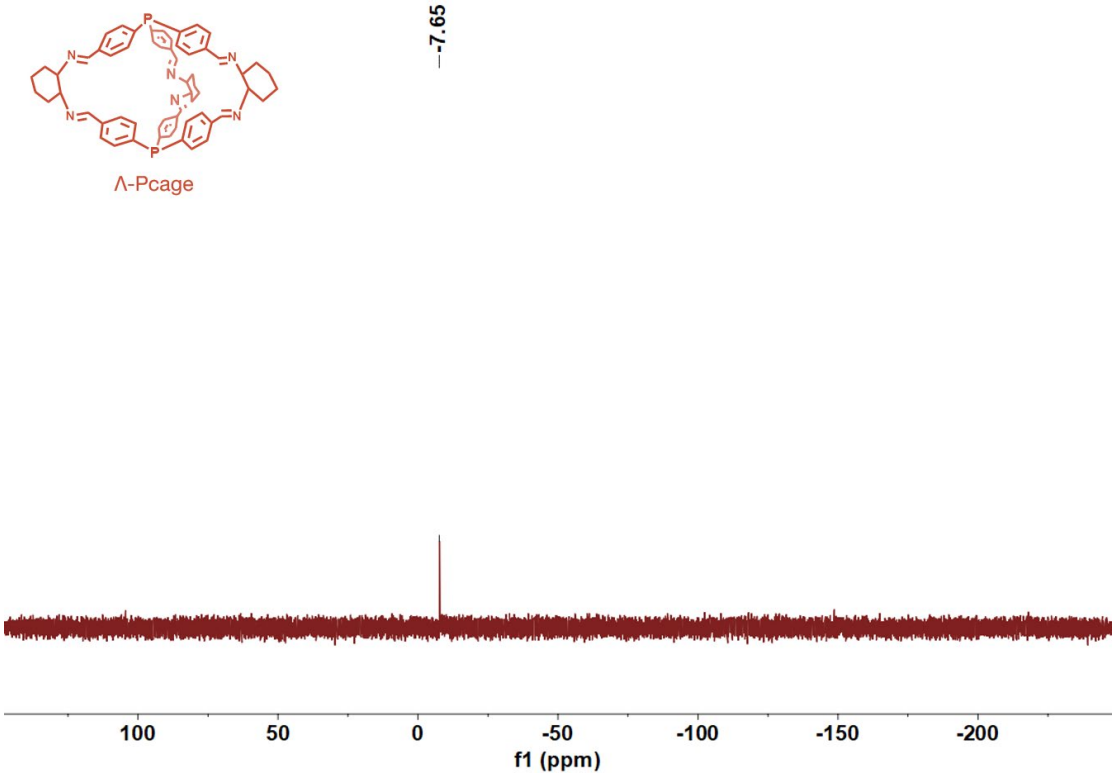

Supplementary Fig. 8 ^{31}P NMR spectra of Λ-Pcage in CD_2Cl_2.

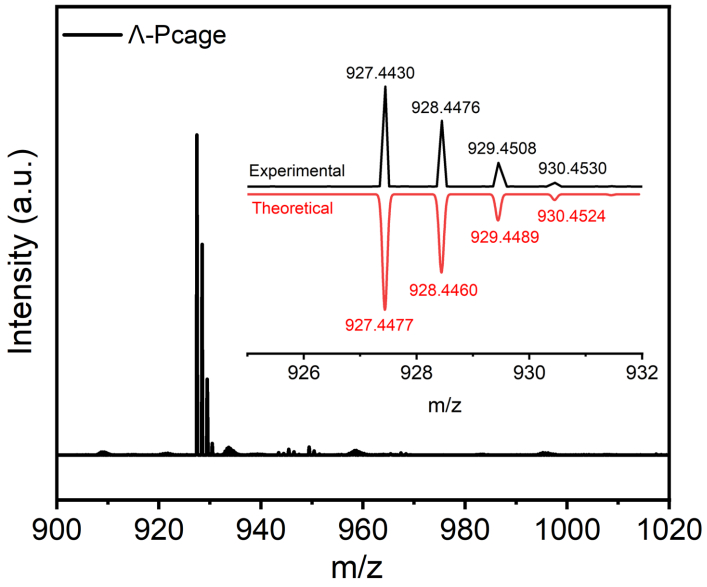

Supplementary Fig. 9 HR-ESI-MS spectrum of Λ-Pcage ($C_{60}H_{60}N_6P_2$, $[M+H]^+$, *m*/*z*, found. 927.4430; calcd. 927.4477).

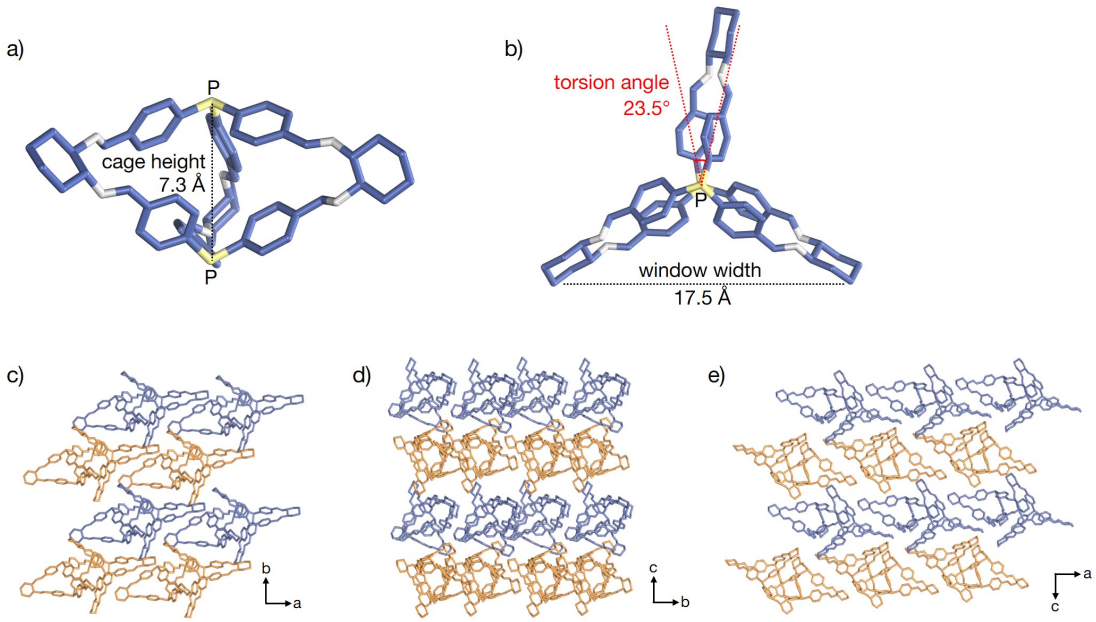

Supplementary Fig. 10 Single crystal structures of left-handed Δ-Pcage: (a) Side view and (b) Top view of Δ-Pcage showing that the height of one single cage is 7.3 Å (distance between two P vertices), the window width is 17.5 Å (distance between two cyclohexane moieties), and the torsion angle is 23.5° (the angle of two P-C bonds between the top and bottom panels). (c-e) Δ-Pcage packing fashion in crystal view along (c) *c*-axis, (d) *a*-axis, and (e) *b*-axis.

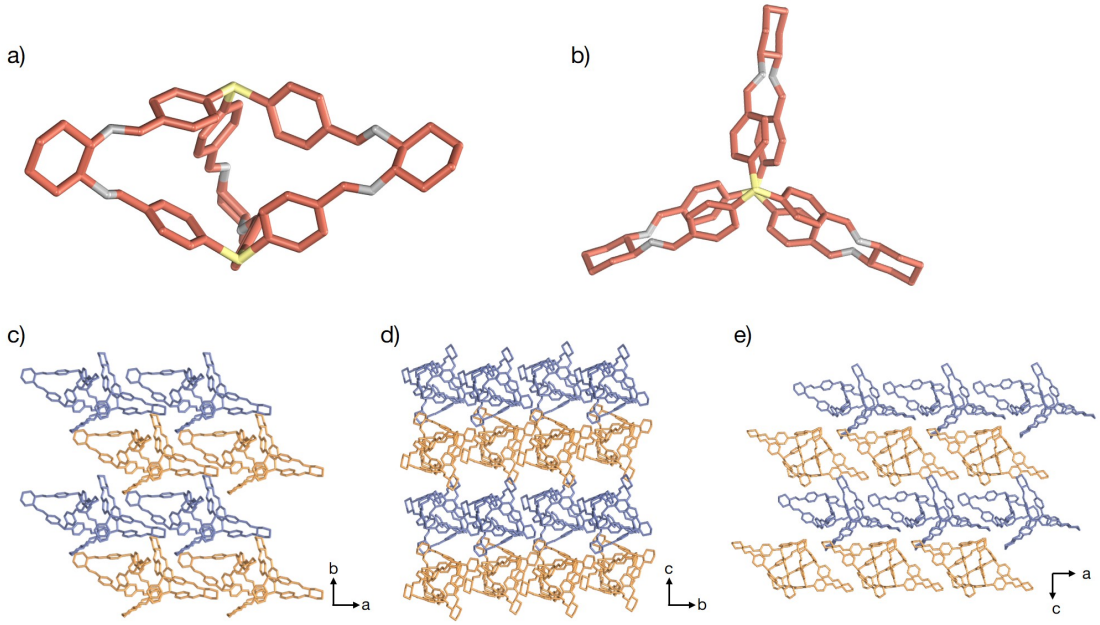

Supplementary Fig. 11 Single crystal structures of right-handed Λ-Pcage: (a) Side view and (b) Top view of Λ-Pcage single crystal. (c-e) Λ-Pcage packing fashion in crystal view along (c) *c*-axis, (d) *a*-axis, and (e) *b*-axis.

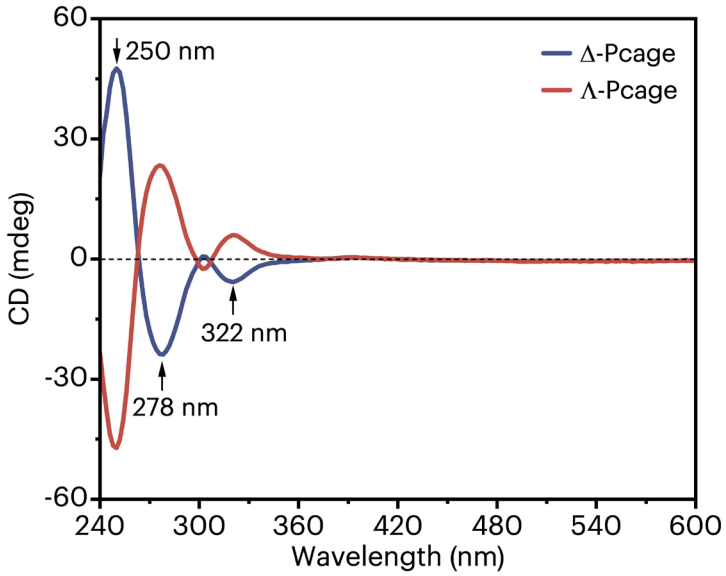

Supplementary Fig. 12 CD spectra of two chiral organic cages, Δ-Pcage (blue curve) and Λ-Pcage (red curve) at room temperature. The concentration of two chiral cages were at 1.0×10^{-5} M.

Circular dichroism (CD) spectra showed that the two organic cages gave strong Cotton effect at 250, 278, and 322 nm with a mirrored sign, confirming that they are enantiomers.

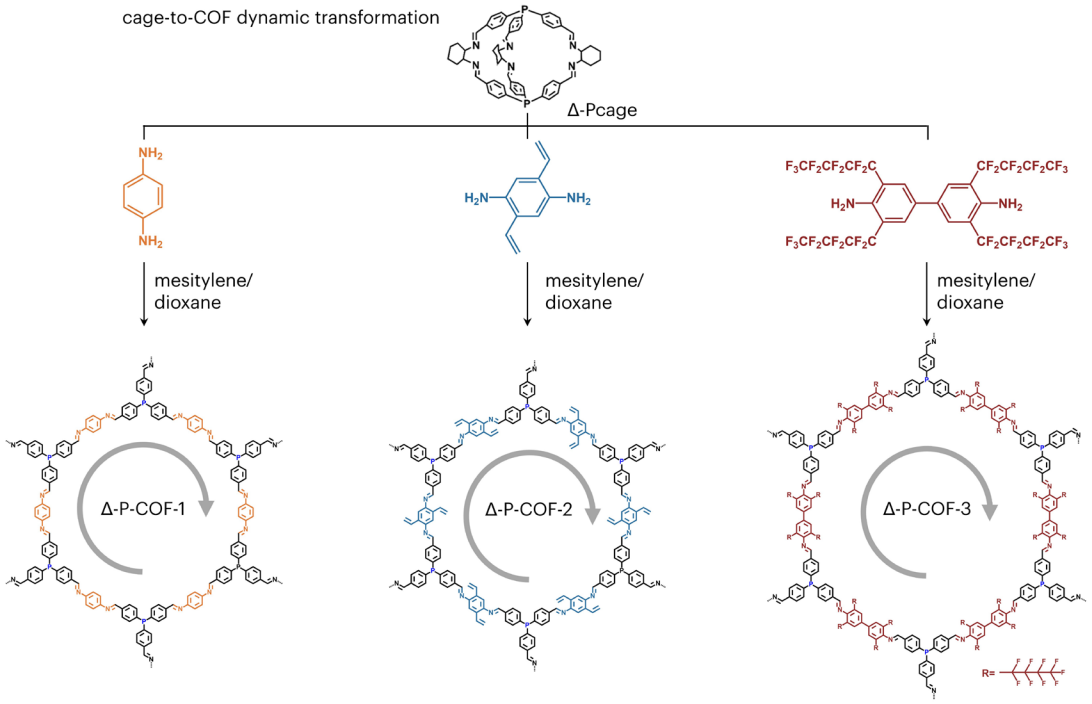

Supplementary Fig. 13 Synthetic routes of chiral P-COF series (Δ-P-COF-1, Δ-P-COF-2, and Δ-P-COF-3) via dynamic conversion from chiral cage to COF structure through chiral memory and transfer.

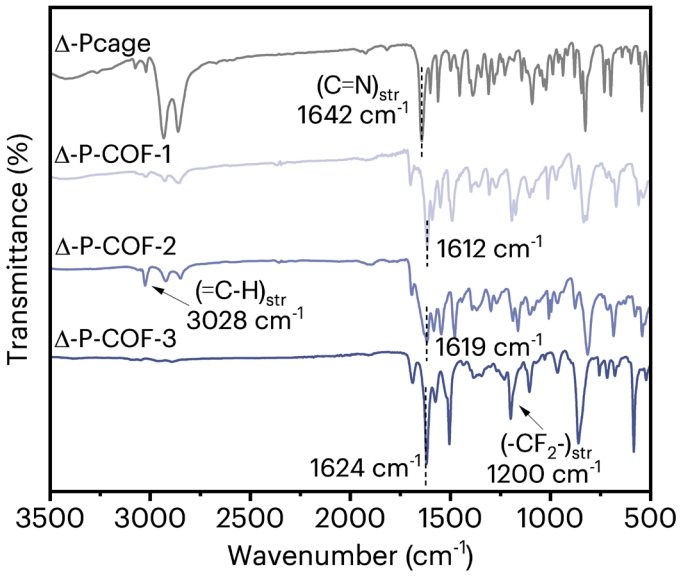

Supplementary Fig. 14 FT-IR spectral change from chiral cage (Δ-Pcage) to chiral P-COF series (Δ-P-COF-1, Δ-P-COF-2, and Δ-P-COF-3).

It was observed that Δ-Pcage has a sharp band at 1642 cm^{-1}, assigned to the stretching vibration of C=N bond adjacent to the alicyclic group in the cage. However, after reaction with different diamine linkers, this band gave characteristic downfield shift to 1612–1624 cm^{-1} (1612 cm^{-1} for Δ-P-COF-1, 1619 cm^{-1} for Δ-P-COF-2, and 1624 cm^{-1} for Δ-P-COF-3), which are ascribed to the aromatic C=N stretching bands, suggesting the successful cage-to-COF structural transformation.

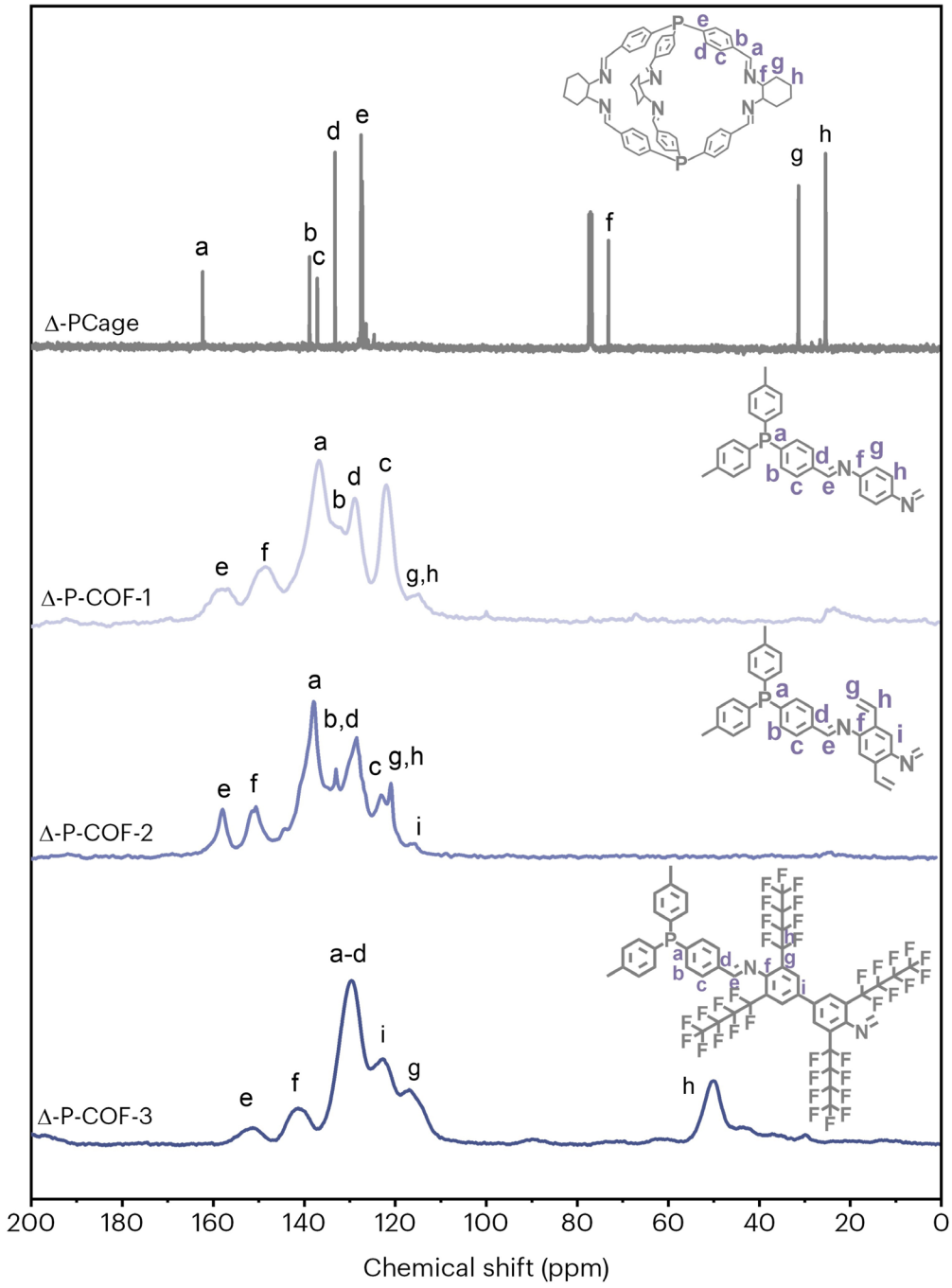

Supplementary Fig. 15 ^{13}C CP-MAS solid-state NMR spectra of chiral cage (Δ-Pcage) and chiral P-COF series (Δ-P-COF-1, Δ-P-COF-2, and Δ-P-COF-3).

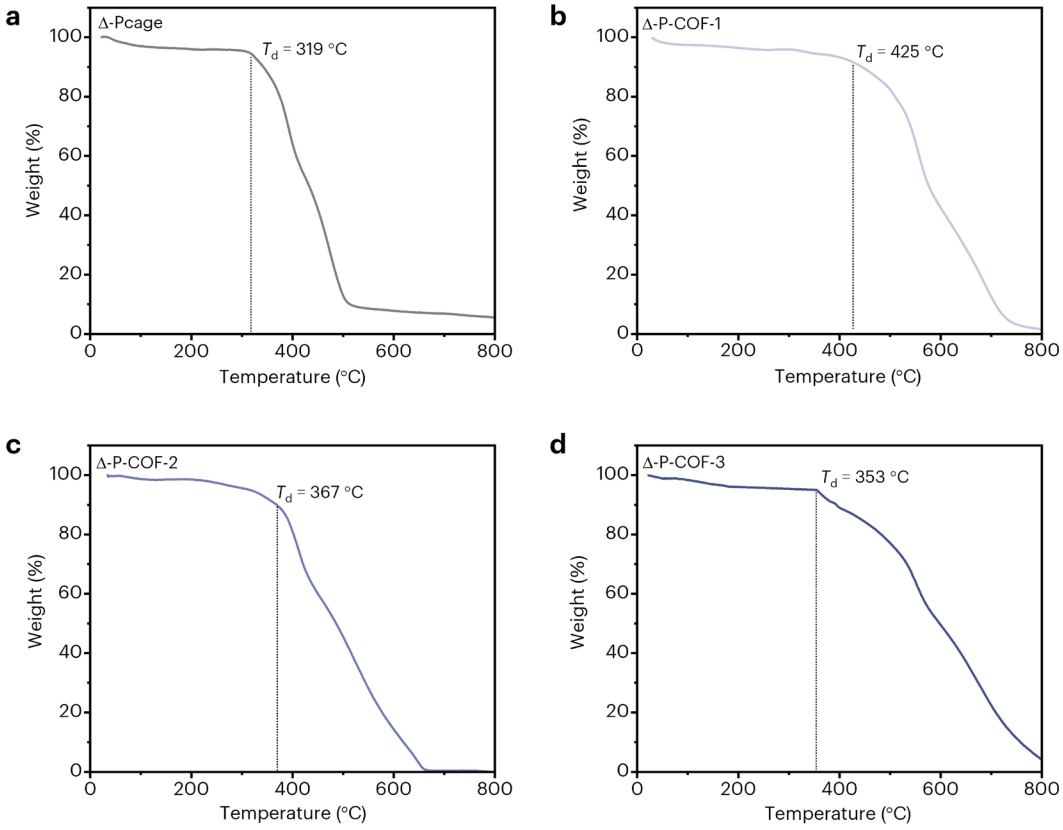

Supplementary Fig. 16 TGA analysis of chiral cage (Δ-Pcage) and chiral P-COF series (Δ-P-COF-1, Δ-P-COF-2, and Δ-P-COF-3).

The decomposition temperature (T_d) of Δ-Pcage is measured to be 319 °C. In comparison, the three kinds of chiral P-COFs showed improved T_d above 350 °C, which indicates that the corresponding chiral P-COF series possess better structural stability and suitable for the piezoelectric applications. Among them, Δ-P-COF-1 gave the highest T_d of 425 °C, while Δ-P-COF-3 was the lowest of 353 °C. This decrease results from the multiple long fluorocarbon grafted onto the COF.

S2. Supplementary characterization of crystalline structures and chiral properties of chiral P-COFs and its achiral counterparts.

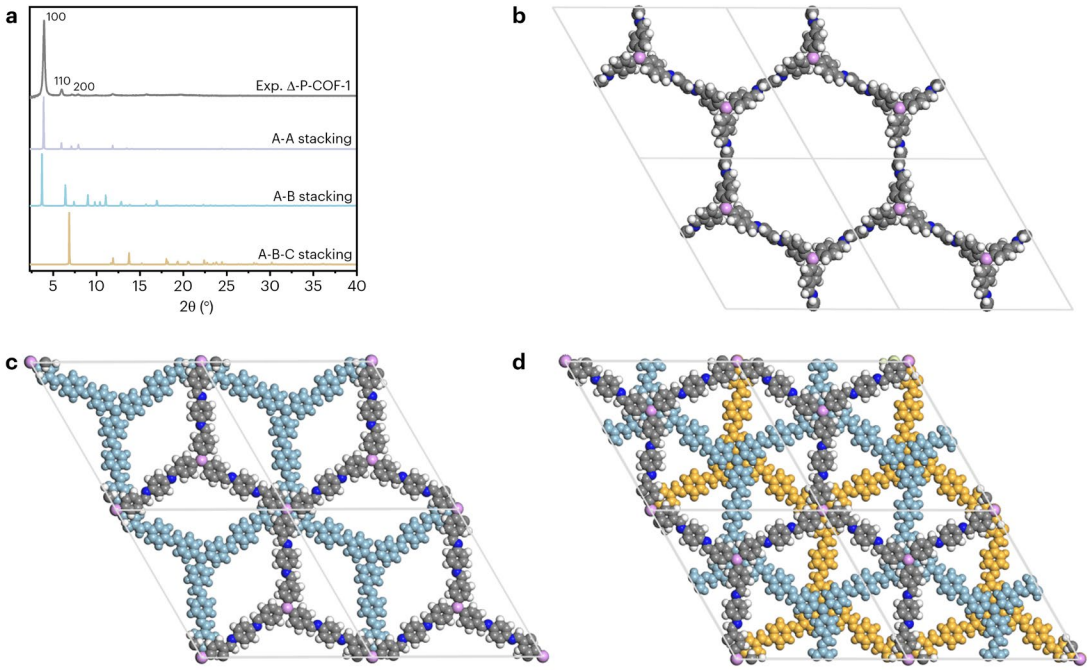

Supplementary Fig. 17 The simulated PXRD of Δ-P-COF-1 based on different stacking fashions. a. The experimental PXRD profiles of Δ-P-COF-1 (grey) and calculated patterns according to AA stacking (purple), AB stacking (cyan), and ABC stacking (yellow). b-d. Space-filling models of Δ-P-COF-1 with b. AA stacking mode, c. AB stacking mode, and d. ABC stacking mode. The color of atoms: carbon, gray; nitrogen, blue; phosphorus, pink.

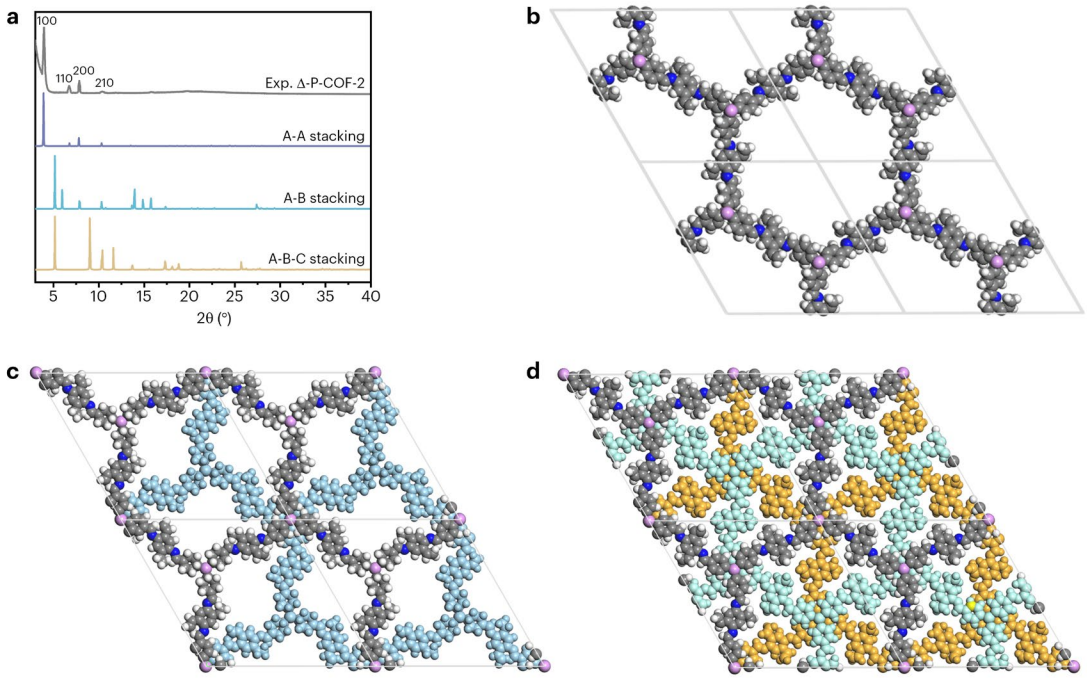

Supplementary Fig. 18 The simulated PXRD of Δ-P-COF-2 based on different stacking fashions. a. The experimental PXRD profiles of Δ-P-COF-2 (grey) and calculated patterns according to AA stacking (purple), AB stacking (cyan), and ABC stacking (yellow). b-d. Space-filling models of Δ-P-COF-2 with b. AA stacking mode, c. AB stacking mode, and d. ABC stacking mode. The color of atoms: carbon, gray; nitrogen, blue; phosphorus, pink.

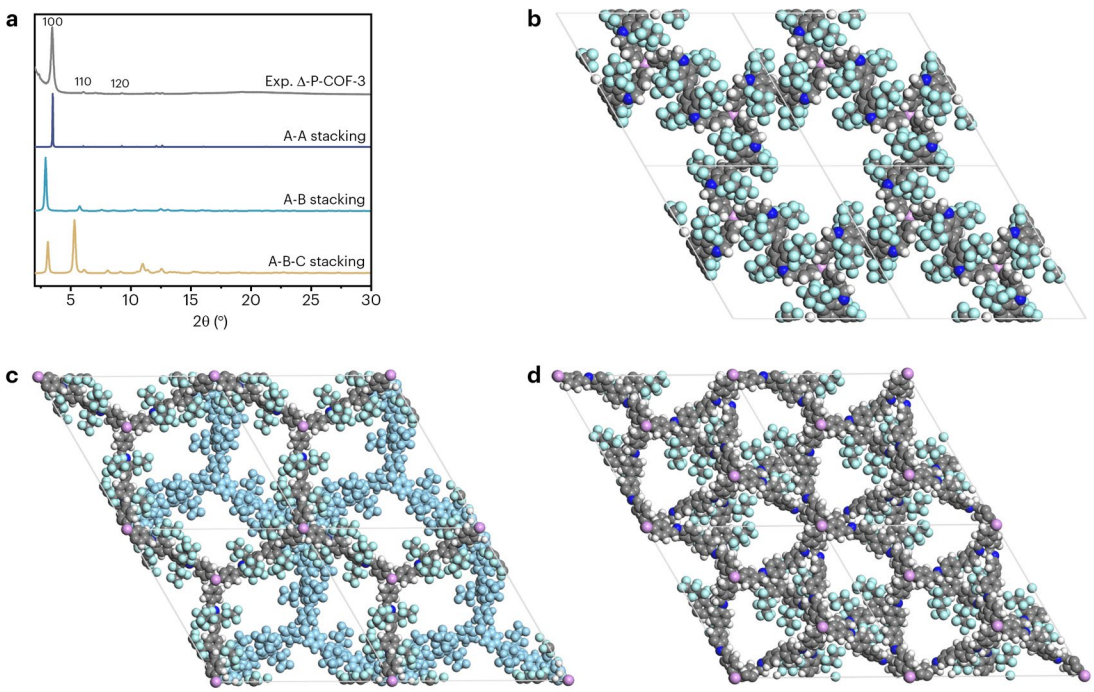

Supplementary Fig. 19 The simulated PXRD of Δ-P-COF-3 based on different stacking fashions. a. The experimental PXRD profiles of Δ-P-COF-3 (grey) and calculated patterns according to AA stacking (purple), AB stacking (cyan), and ABC stacking (yellow). b-d. Space-filling models of Δ-P-COF-3 with b. AA stacking mode, c. AB stacking mode, and d. ABC stacking mode. The color of atoms: carbon, gray; nitrogen, blue; fluorine, cyan; phosphorus, pink.

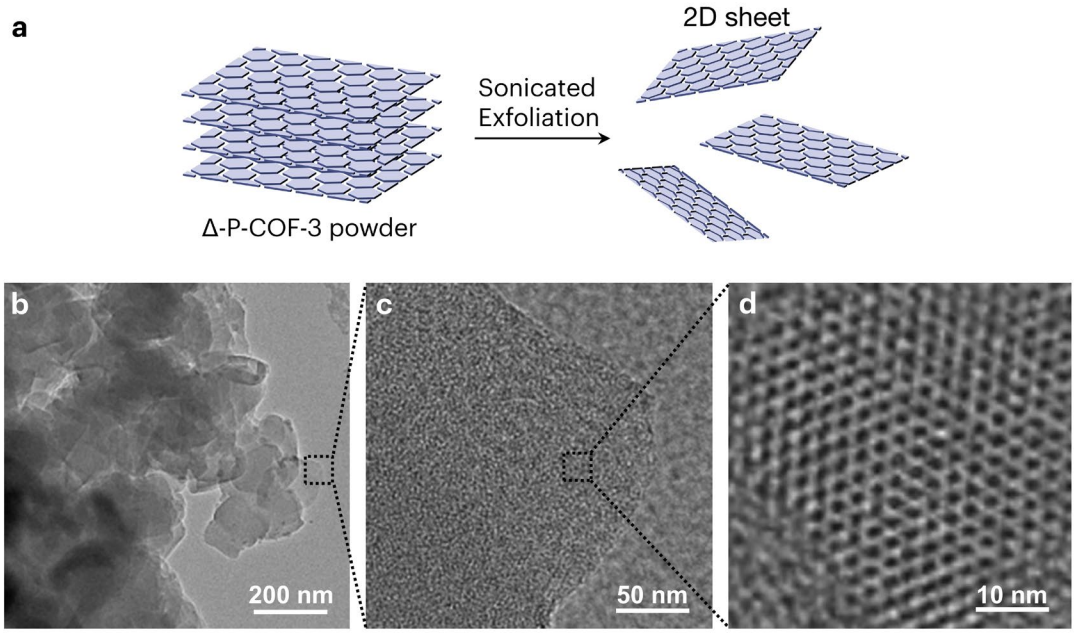

Supplementary Fig. 20 2D layered architecture of Δ-P-COF-3 by sonicated exfoliation. a. Schematic illustration of the exfoliation of Δ-P-COF-3 solid powder into 2D sheets through strong sonication. b-d. TEM images of the 2D sheet-like structure of Δ-P-COF-3 with high-resolution visualization.

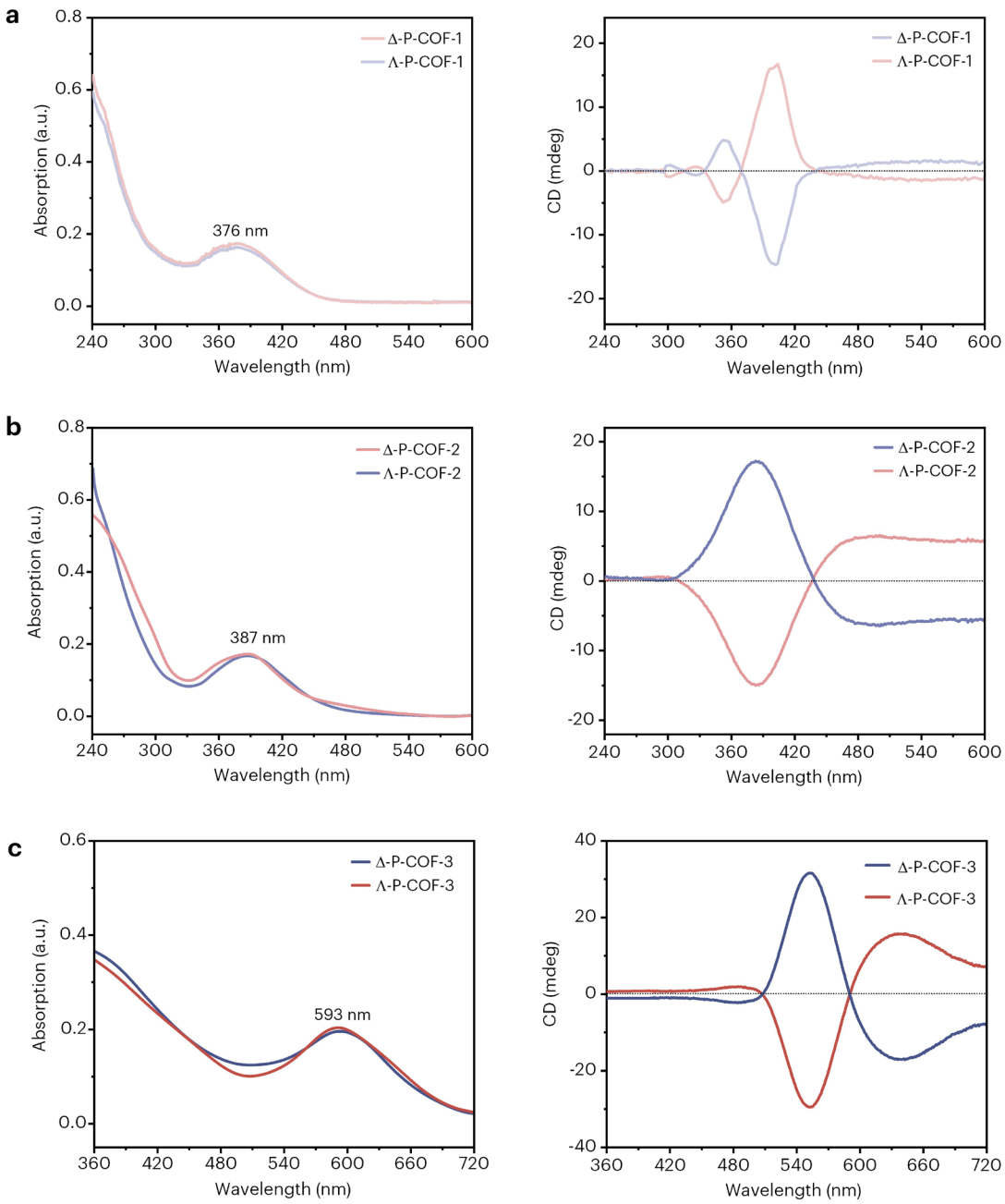

Supplementary Fig. 21 a-c. UV-vis spectra (left panels) and corresponding CD spectra (right panels) of chiral P-COFs in solutions (1.0×10^{-5} M): a. Δ-P-COF-1 and Λ-P-COF-1, b. Δ-P-COF-2 and Λ-P-COF-2, and c. Δ-P-COF-3 and Λ-P-COF-3.

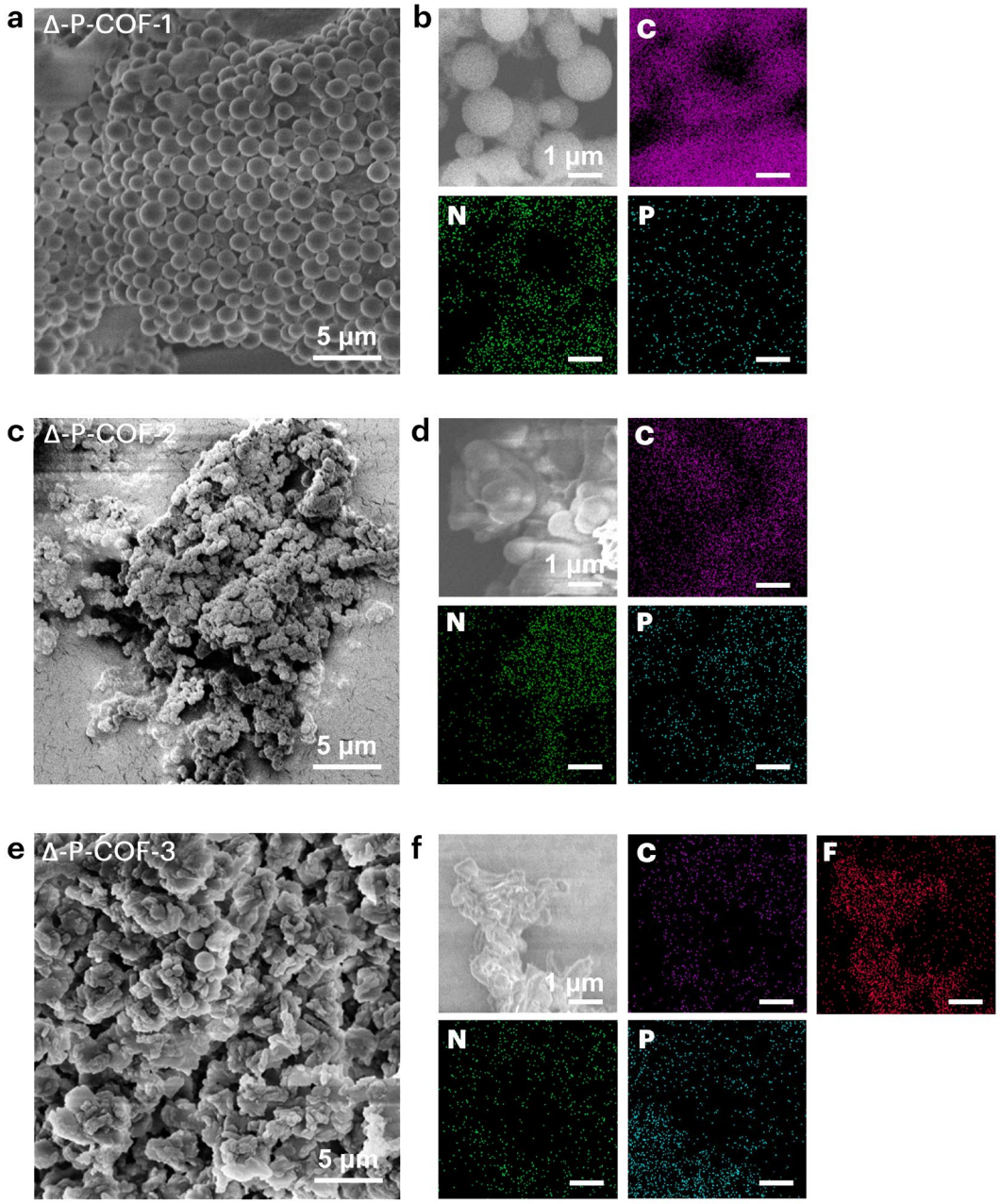

Supplementary Fig. 22 a,c,e. SEM images of chiral P-COF series: a. Δ-P-COF-1, c. Δ-P-COF-2, and e. Δ-P-COF-3 (scale bar, 5 μm). b,d,f. EDS mapping of chiral P-COF series: b. Δ-P-COF-1, d. Δ-P-COF-2, and f. Δ-P-COF-3 (scale bar, 1 μm).

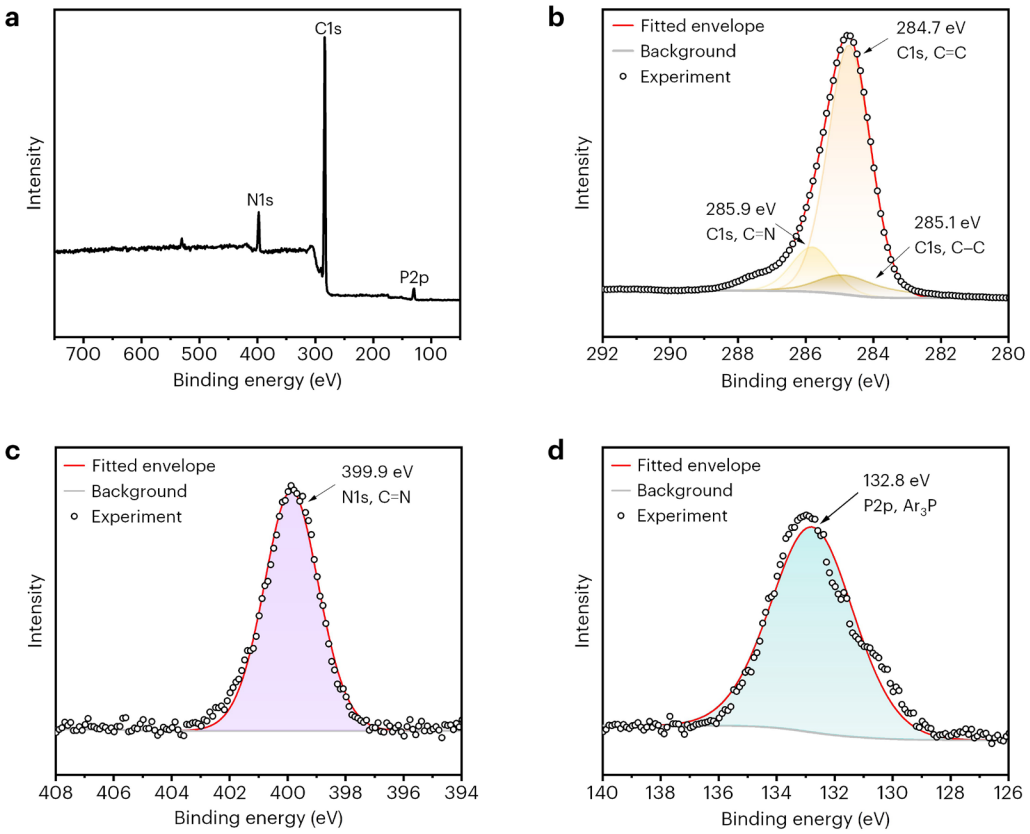

Supplementary Fig. 23 XPS spectra of Δ-P-COF-1: a. Total XPS spectrum, b. The C1s spectrum (C=C, 284.7 eV; C–C, 285. 1 eV, C=N, 285.9 eV), c. The N1s spectrum (C=N, 399.9 eV), d. The P2p spectrum (Ar–P, 132.8 eV).

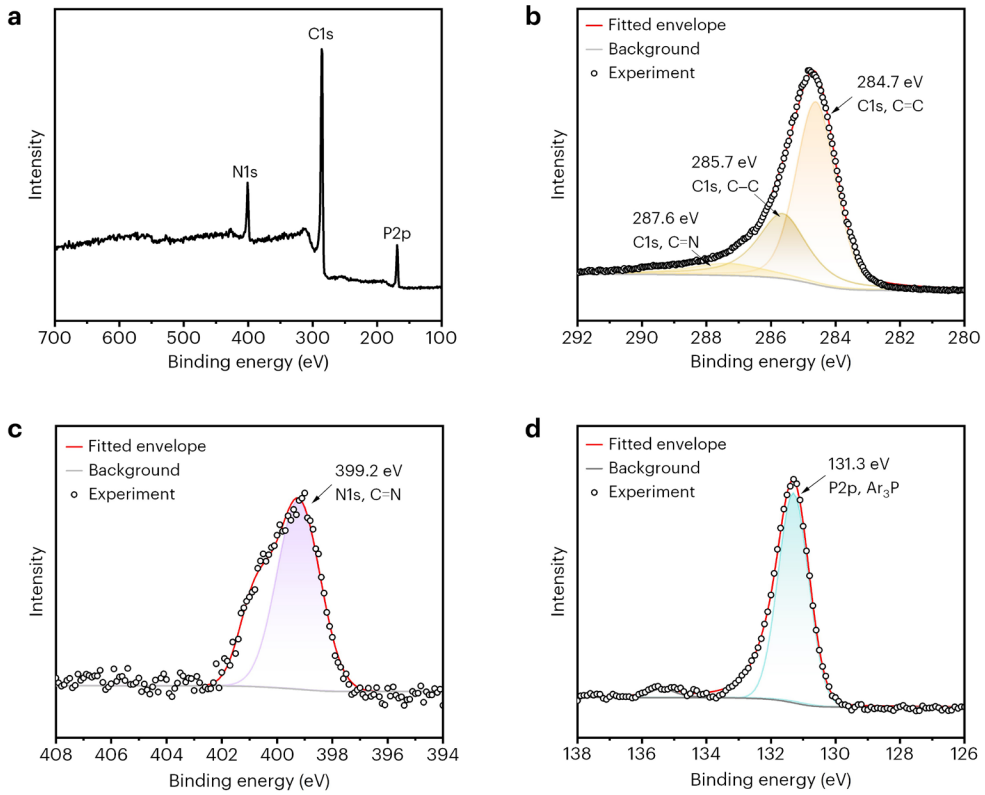

Supplementary Fig. 24 XPS spectra of Δ-P-COF-2: a. Total XPS spectrum, b. The C1s spectrum (C=C, 284.7 eV; C–C, 285. 7 eV, C=N, 287.6 eV), c. The N1s spectrum (C=N, 399.2 eV), d. The P2p spectrum (Ar–P, 131.3 eV).

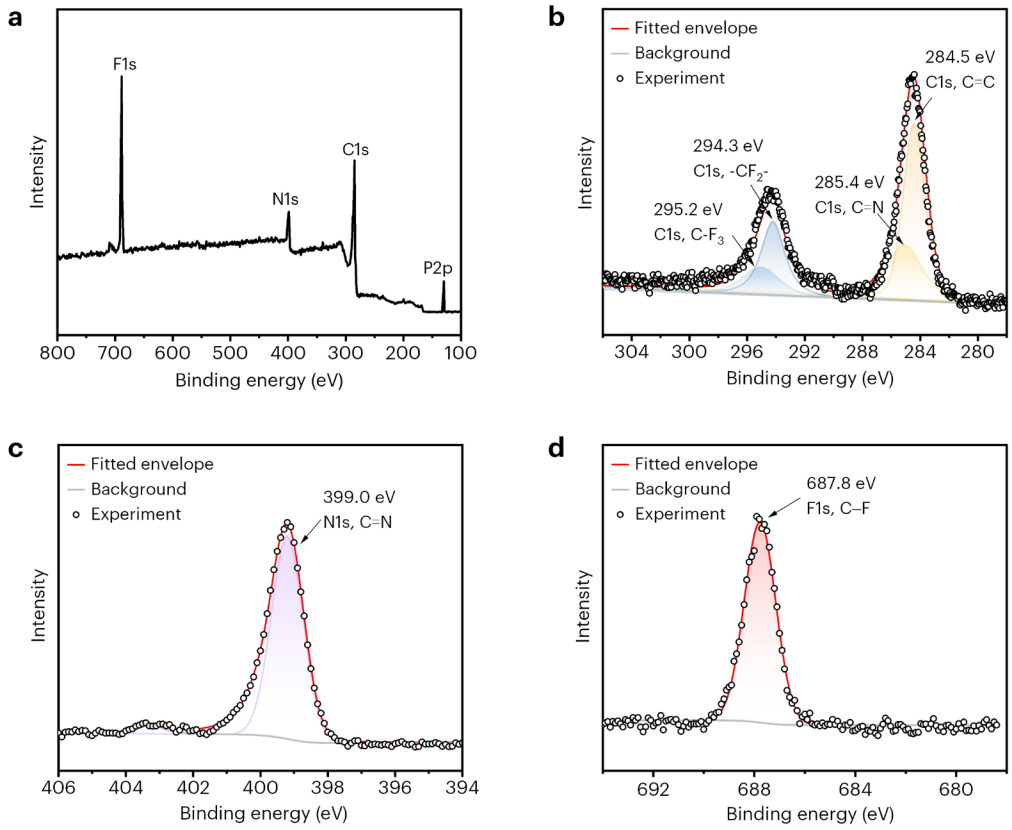

Supplementary Fig. 25 XPS spectra of Δ-P-COF-3: a. Total XPS spectrum, b. The C1s spectrum (C=C, 284.5 eV; C=N, 285.4 eV; C–F_2, 294.3 eV; C–F_3, 295.2 eV), c. The N1s spectrum (C=N, 399.0 eV), d. The F1s spectrum (C–F, 687.8 eV).

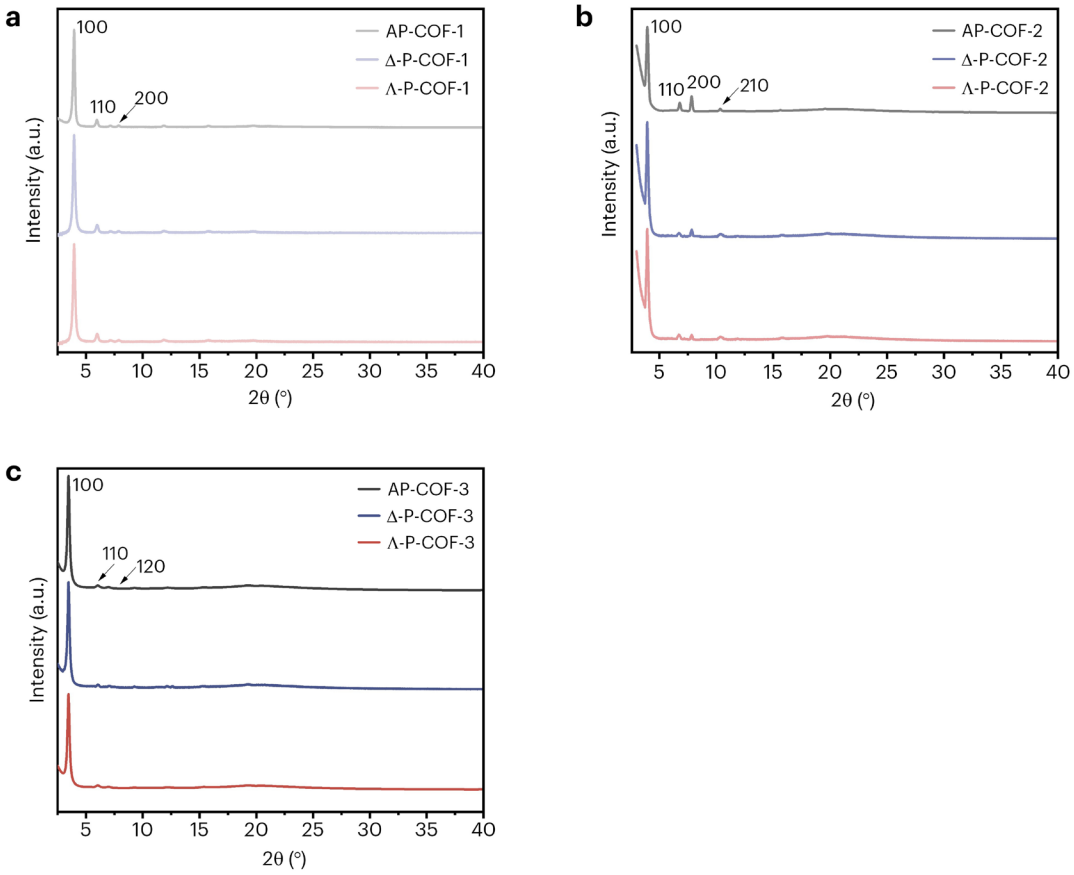

Supplementary Fig. 26 The experimental PXRD profiles of achiral AP-COF counterparts compared with the corresponding chiral ones: a. AP-COF-1 with Δ- and Λ-P-COF-1, b. AP-COF-2 with Δ- and Λ-P-COF-2, c. AP-COF-3 with Δ- and Λ-P-COF-3.

From the PXRD patterns, it was found that there was no apparent difference between these fully eclipsed tabular stacking of AP-COFs and the torsional propeller stacking of chiral P-COFs, as the chirality would only affect the relative intensity and width of certain diffraction peaks and peak position at small *d*-spacings.

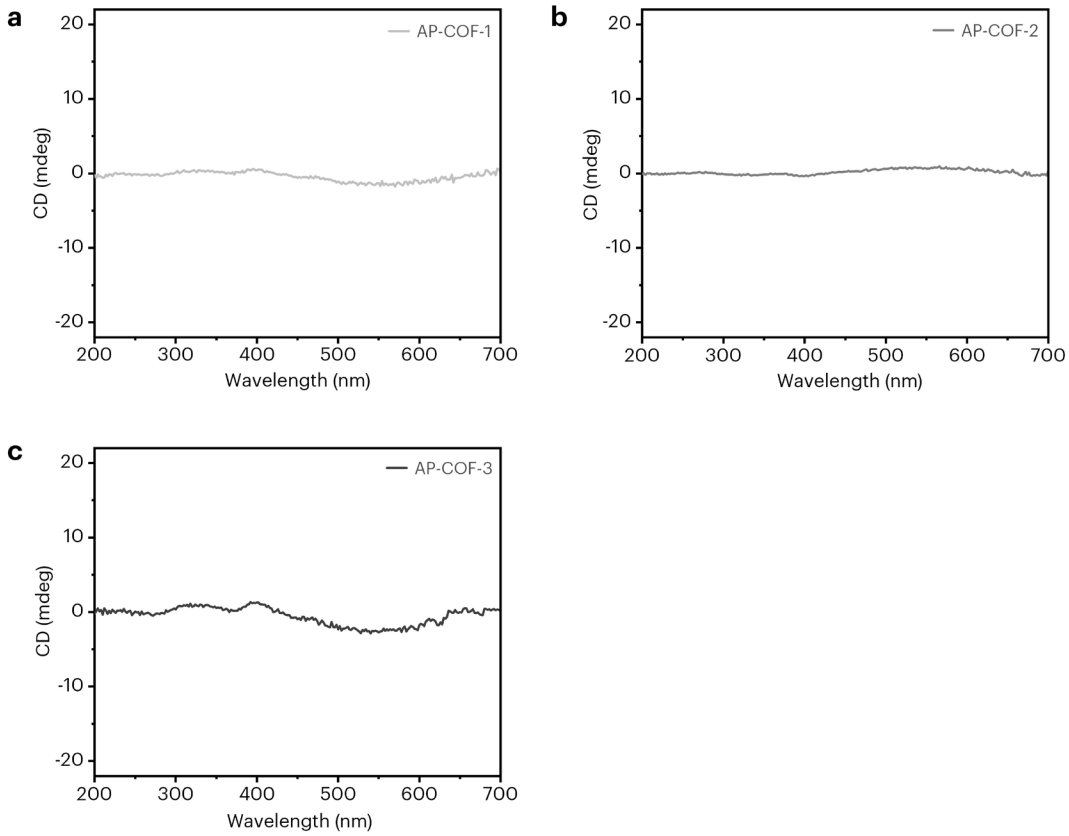

Supplementary Fig. 27 CD spectral signals of achiral AP-COF counterparts in solutions (1.0×10^{-5} M): a. AP-COF-1, b. AP-COF-2, c. AP-COF-3.

From the CD spectra, it was observed that all the achiral AP-COF series had no obvious CD signals, indicating that they are typically non-chiral COF structures.

S3. Supplementary measurements on piezoelectric properties of chiral P-COFs and its achiral counterparts.

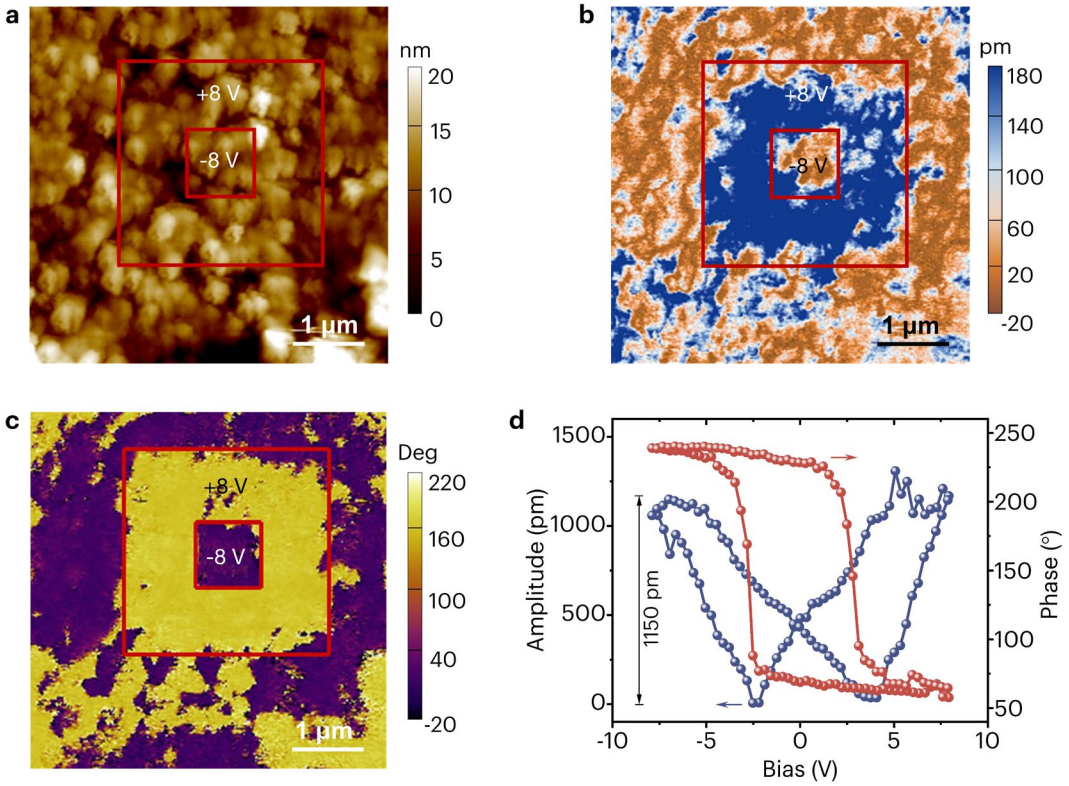

Supplementary Fig. 28 Ferroelectric domain switching of Δ-P-COF-3: a. Topography of a box-in-box domain pattern in Δ-P-COF-3 thin-film. The pattern was applied a tip voltage of +8 V and -8 V to a single-domain state. b. Amplitude image of the box-in-box domain pattern in Δ-P-COF-3 thin-film. c. Phase image of the box-in-box domain pattern in Δ-P-COF-3 thin-film. d. PFM switching spectroscopy for phase hysteresis loop (red circles) and amplitude loop (blue circles) on a local site of Δ-P-COF-3 film.

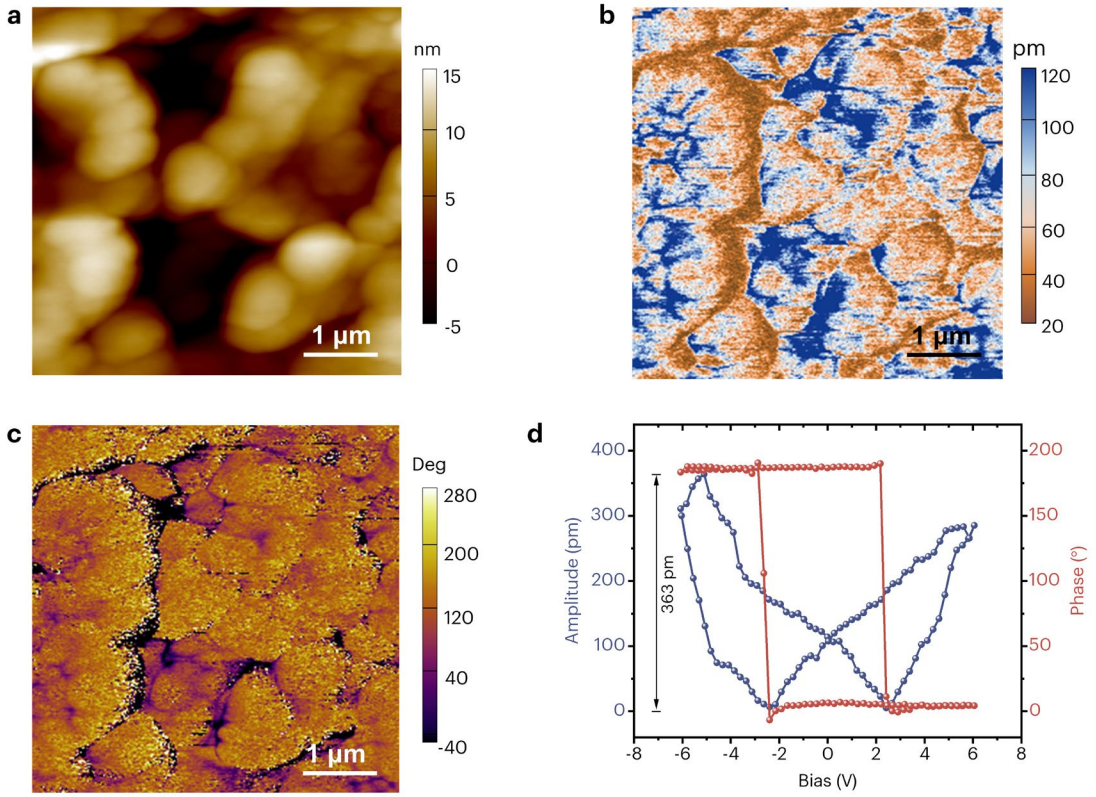

Supplementary Fig. 29 Lateral PFM images of Δ-P-COF-3: a. Topographic image. b. Amplitude image. c. Phase image. d. PFM switching spectroscopy for phase hysteresis loop (red circles) and amplitude loop (blue circles).

From the lateral PFM characterization, it can be seen that the maximal amplitude is 363 pm, much weaker than that of vertical PFM (1150 pm). This indicates that the in-plane piezoelectric response is significantly weaker than its out-of-plane piezoelectricity of Δ-P-COF-3 thin-film.

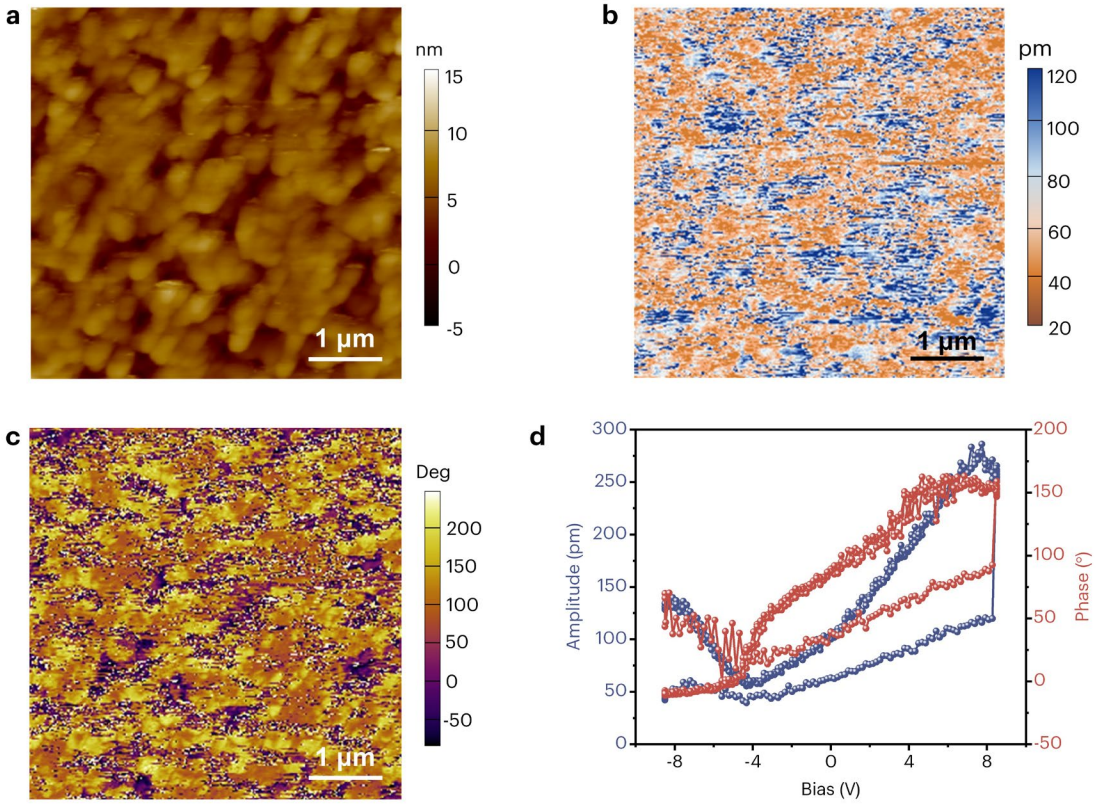

Supplementary Fig. 30 Vertical PFM images of achiral COF counterpart, AP-COF-3: a. Topography. b. Amplitude image. c. Phase image. d. PFM switching spectroscopy for phase hysteresis loop (red circles) and amplitude loop (blue circles).

The achiral AP-COF-3 counterpart was studied under the same conditions. However, its vertical PFM showed smaller and irregular-shaped domains, and meanwhile, the phase and amplitude hysteresis loops were ill-defined, which indicate that AP-COF-3 has much weaker piezoelectric response as compared to that of chiral Δ-P-COF-3, even though AP-COF-3 also carries the identical high-polar fluorocarbon grafts on its structure. These results further validate our hypothesis that the ordering orientation of polar groups induced by homochiral COF plays a crucial role in amplifying the piezoelectric effect.

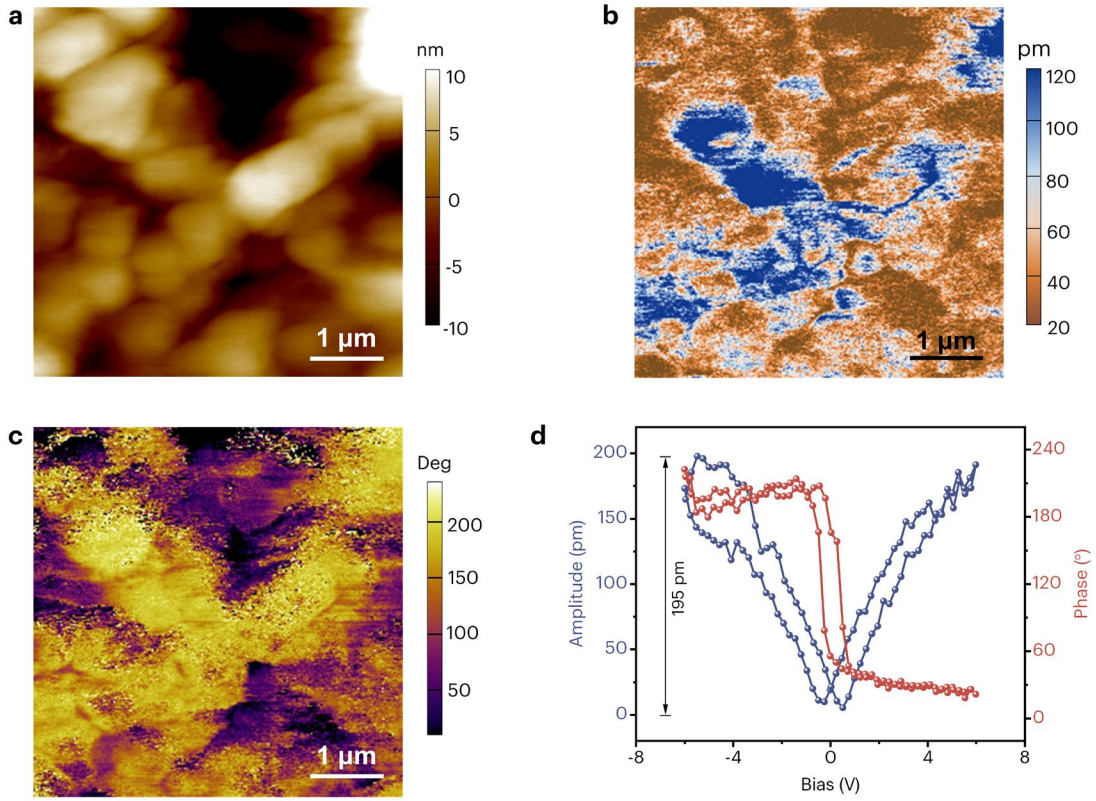

Supplementary Fig. 31 Vertical PFM measurements of Δ-P-COF-1: a. Topography. b. Amplitude image. c. Phase image. d. PFM switching spectroscopy for phase hysteresis loop (red circles) and amplitude loop (blue circles).

From the above results, it was found that the piezoelectricity of Δ-P-COF-1 thin-film is significantly lower than that of Δ-P-COF-3, as indicated by the maximal amplitude of 195 pm. The obtained d_{33} value from PFM tests is determined to be 35.8 pm/V, which is only 22% of Δ-P-COF-3 (159.4 pm/V).

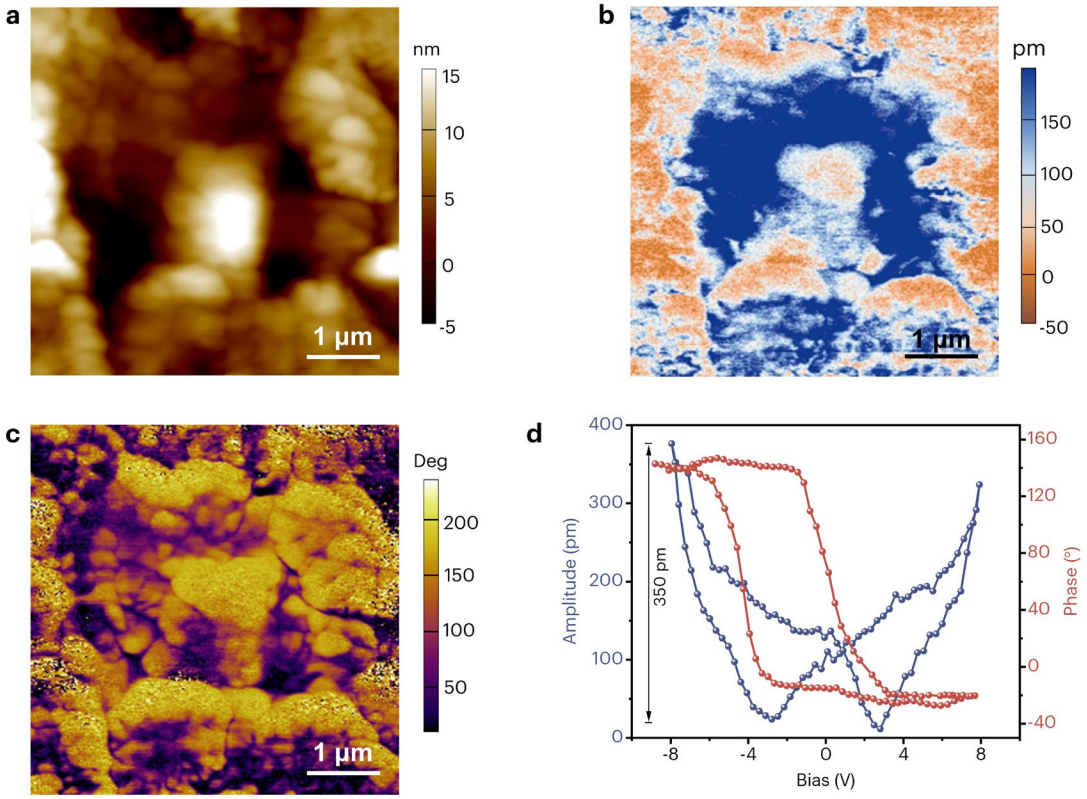

Supplementary Fig. 32 Vertical PFM measurements of Δ-P-COF-2: a. Topography. b. Amplitude image. c. Phase image. d. PFM switching spectroscopy for phase hysteresis loop (red circles) and amplitude loop (blue circles).

It was found that the piezoelectricity of Δ-P-COF-2 thin-film is lower than that of Δ-P-COF-3, as indicated by the maximal amplitude of 350 pm. The obtained d_{33} value from PFM tests is determined to be 61.9 pm/V, which is only 38% of Δ-P-COF-3 (159.4 pm/V).

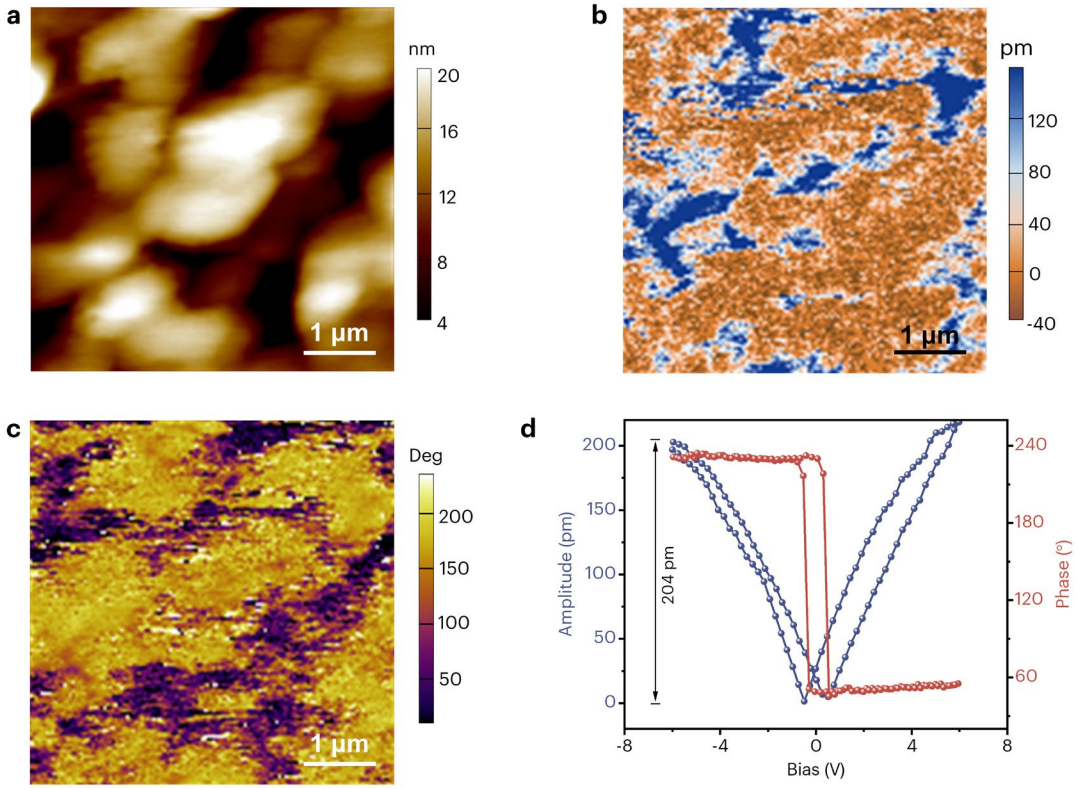

Supplementary Fig. 33 Vertical PFM tests of right-handed Λ-P-COF-1 with opposite homochirality: a. Topography. b. Amplitude image. c. Phase image. d. PFM switching spectroscopy for phase hysteresis loop (red circles) and amplitude loop (blue circles).

The right-handed Λ-P-COF-1 thin-film had the similar PFM amplitude and phase images to that of Δ-P-COF-1 film, and its maximal amplitude in PFM amplitude hysteresis loop is determined to be 204 pm, close to that of Δ-P-COF-1 (195 pm). These results indicate that Λ-P-COF-1 is of similar piezoresponse with its mirrored counterpart, Δ-P-COF-1.

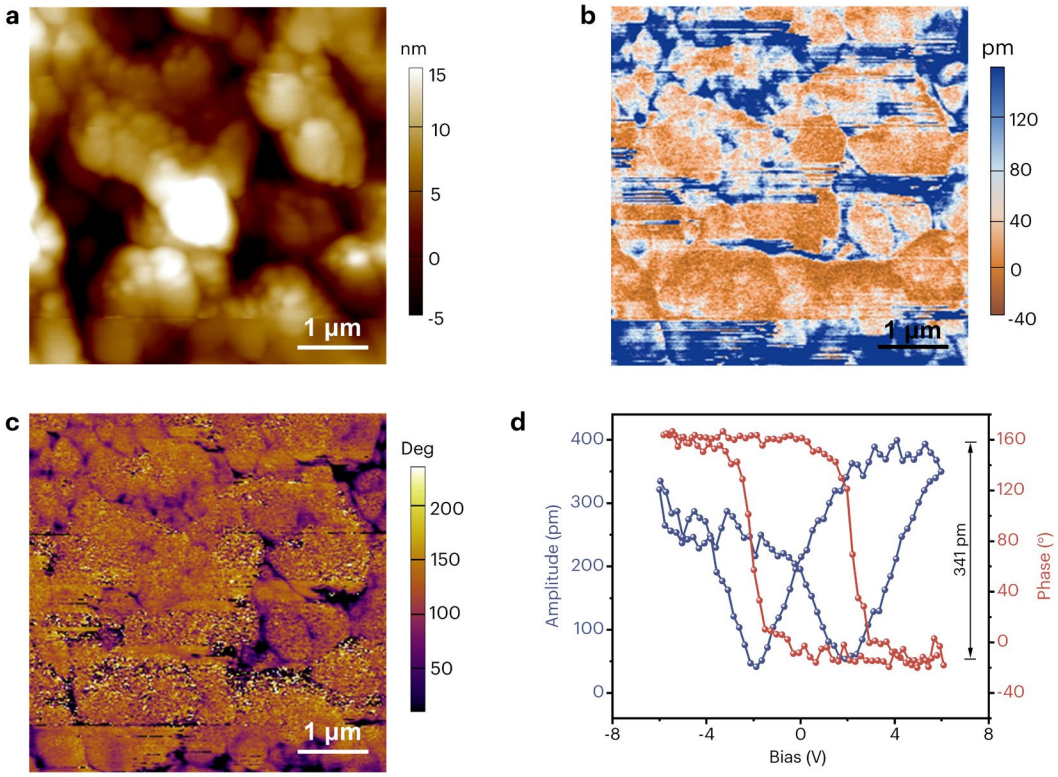

Supplementary Fig. 34 Vertical PFM tests of right-handed Λ-P-COF-2 with opposite homochirality: a. Topography. b. Amplitude image. c. Phase image. d. PFM switching spectroscopy for phase hysteresis loop (red circles) and amplitude loop (blue circles).

The right-handed Λ-P-COF-2 thin-film had the similar PFM amplitude and phase images to that of Δ-P-COF-2 film, and its maximal amplitude in PFM amplitude hysteresis loop is determined to be 341 pm, close to that of Δ-P-COF-2 (350 pm). These results indicate that Λ-P-COF-2 is of similar piezoresponse with its mirrored counterpart, Δ-P-COF-2.

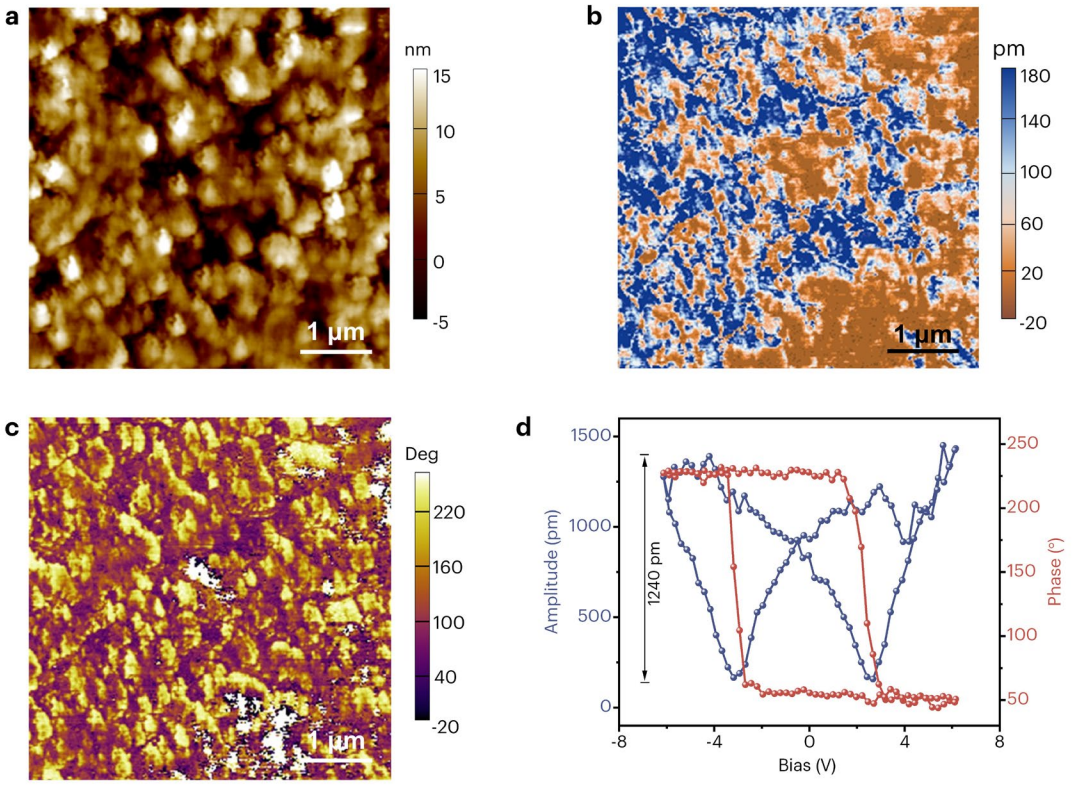

Supplementary Fig. 35 Vertical PFM tests of right-handed Λ-P-COF-3 with opposite homochirality: a. Topography. b. Amplitude image. c. Phase image. d. PFM switching spectroscopy for phase hysteresis loop (red circles) and amplitude loop (blue circles).

The right-handed Λ-P-COF-3 thin-film had the similar PFM amplitude and phase images to that of Δ-P-COF-3 film, and its maximal amplitude in PFM amplitude hysteresis loop is determined to be 1240 pm, approaching the value of Δ-P-COF-3 (1150 pm). These results indicate that Λ-P-COF-3 is of similar piezoresponse with its mirrored counterpart, Δ-P-COF-3.

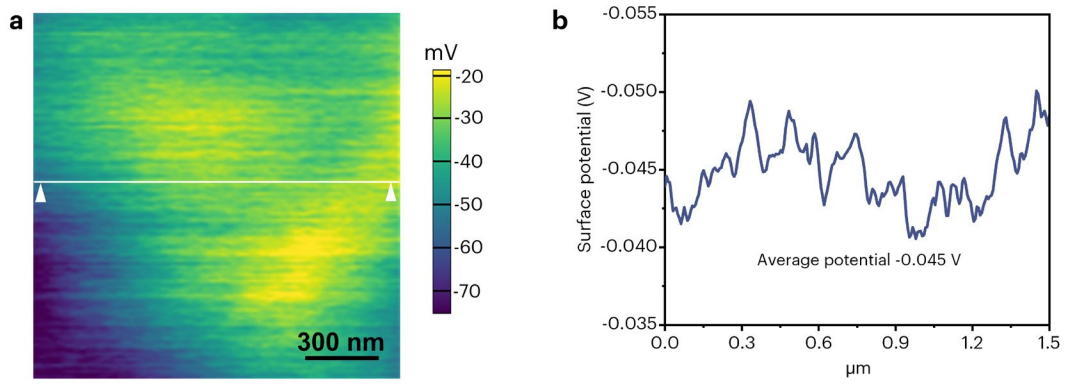

Supplementary Fig. 36 KPFM characterization of the surface potential of Δ-P-COF-1: a. KPFM surface potential image. b. The corresponding surface potential curve along the white line.

From the surface potential image and corresponding potential profile, it was evidenced that Δ-P-COF-1 gave an average −0.045 V surface potential, which is only one-sixth than that of Δ-P-COF-3 (average −0.26 V).

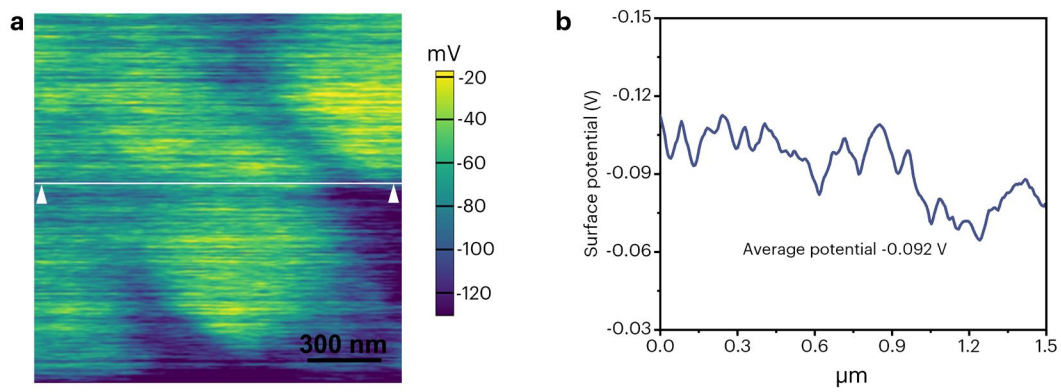

Supplementary Fig. 37 KPFM characterization of the surface potential of Δ-P-COF-2: a. KPFM surface potential image. b. The corresponding surface potential curve along the white line.

From the surface potential image and corresponding potential profile, it was evidenced that Δ-P-COF-2 appeared an average −0.092 V surface potential, which is smaller than that of Δ-P-COF-3 (average −0.26 V).

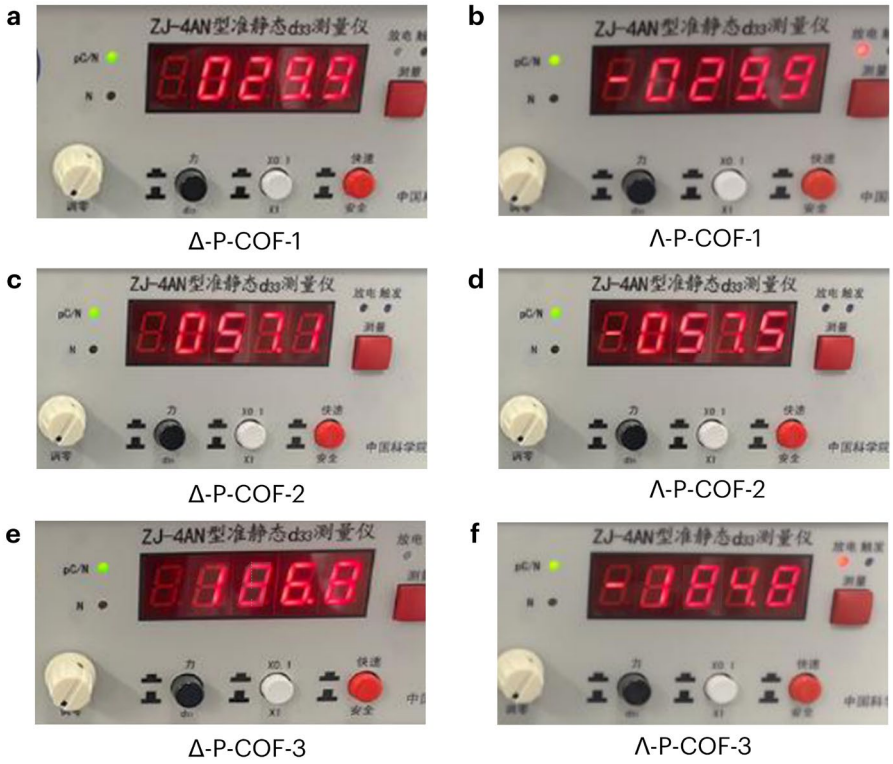

Supplementary Fig. 38 Quasi-static measurements of piezoelectric constant d_{33} of chiral P-COF thin-film materials based on Berlincourt method. a, c, e. Δ-isoforms of chiral P-COFs: a. Δ-P-COF-1 (29.9 pC/N), c. Δ-P-COF-2 (57.1 pC/N), and e. Δ-P-COF-3 (186.8 pC/N). b, d, f. Λ-isoforms of chiral P-COFs: b. Λ-P-COF-1 (−29.9 pC/N), d. Λ-P-COF-2 (−57.5 pC/N), and f. Λ-P-COF-3 (−184.8 pC/N).

S4. Theoretical simulation of 3D elastic moduli of chiral P-COFs.

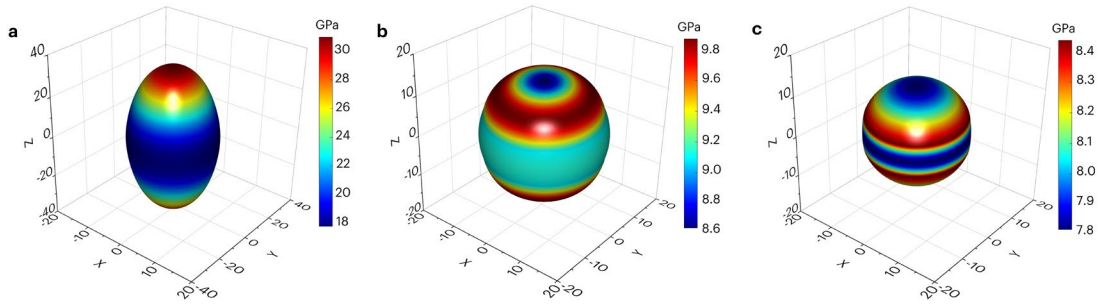

Supplementary Fig. 39 3D plots of elastic modulus of chiral Δ-P-COF-1. a. Directional Young's modulus, b. Spatial dependence of shear modulus MAX, c. Spatial dependence of shear modulus MIN.

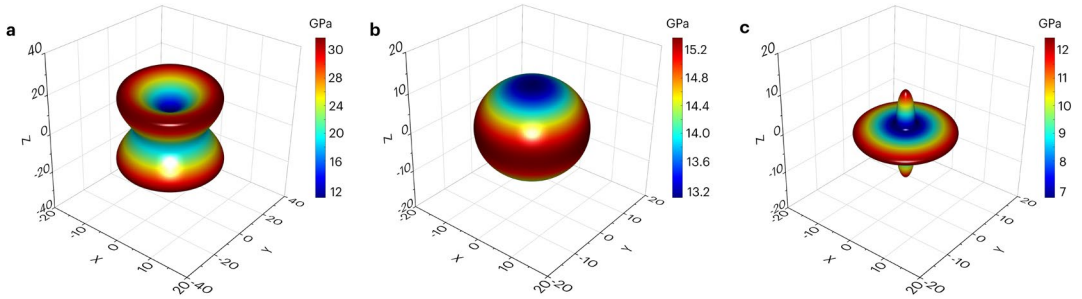

Supplementary Fig. 40 3D plots of elastic modulus of chiral Δ-P-COF-2. a. Directional Young's modulus, b. Spatial dependence of shear modulus MAX, c. Spatial dependence of shear modulus MIN.

S5. Supplementary tests on piezoelectric effect of chiral P-COF/PDMS composite devices.

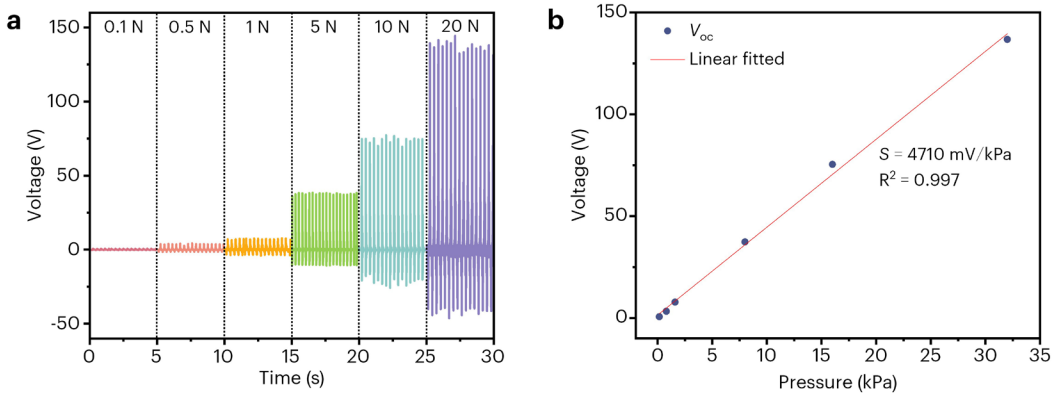

Supplementary Fig. 41 Output voltage of Δ-P-COF-3/PDMS composite piezoelectric device and mechanical-to-electrical sensing sensitivity. a. The output voltages of Δ-P-COF-3/PDMS composite device under different applied force conditions (0.1–20 N, equal to 0.16–32 kPa). b. Linear relationship between the output voltage and the applied pressure.

It was found that the output voltage rises linearly with the external force from 0.1 to 20 N (0.16 to 32 kPa), and the pressure sensitivity ($S = \Delta V/\Delta P$) is fitted to be 4710 mV/kPa.

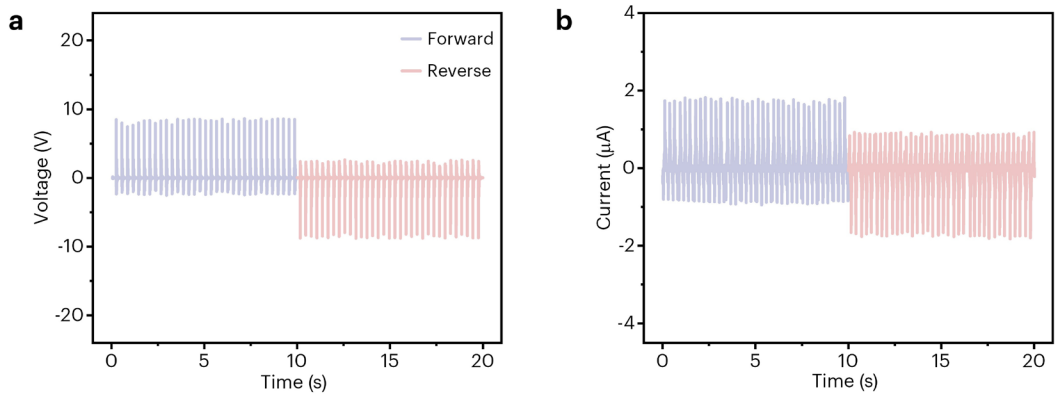

Supplementary Fig. 42 The piezoelectric output performance of Δ-P-COF-1/PDMS composite PENG device. a. The V_{oc} of Δ-P-COF-1/PDMS composite device (8.0 V). b. The I_{sc} of Δ-P-COF-1/PDMS composite device (1.7 μA).

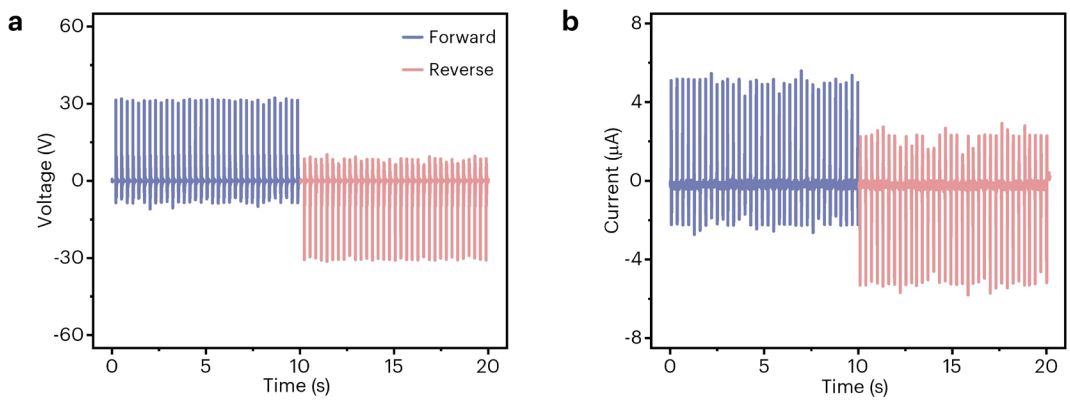

Supplementary Fig. 43 The piezoelectric output performance of Δ-P-COF-2/PDMS composite PENG device. a. The V_{oc} of Δ-P-COF-2/PDMS composite device (31 V). b. The I_{sc} of Δ-P-COF-2/PDMS composite device (4.9 μA).

Supplementary Table 1. Crystallographic data obtained from the Δ-Pcage.

Empirical formula	$C_{60.5}H_{63}N_6OP_2$
Formula weight	952.11
Temperature/K	173.00
Crystal system	monoclinic
Space group	C2
a/Å	20.0068(5)
b/Å	23.3930(5)
c/Å	25.7506(6)
α/°	90
β/°	98.0570(10)
γ/°	90
Volume/Å^3	11932.8(5)
Z	8
ρ_{calc}g/cm^3	1.060
μ/mm^{-1}	0.635
F(000)	4048.0
Crystal size/mm^3	0.27 × 0.23 × 0.21
Radiation	GaK$_\alpha$ (λ = 1.34139)
2θ range for data collection/°	2.543 to 59.496
Index ranges	$-25 \le h \le 25$, $-30 \le k \le 30$, $-33 \le l \le 33$
Reflections collected	139884
Independent reflections	26324 [R_{int} = 0.0437]
Data/restraints/parameters	26324/21/1271
Goodness-of-fit on F^2	1.024
Final R indexes [$I \ge 2\sigma(I)$]	R_1 = 0.0445, wR_2 = 0.1180
Final R indexes [all data]	R_1 = 0.0508, wR_2 = 0.1231
Largest diff. peak/hole/e Å^{-3}	0.46/-0.25
Flack parameter	0.041(4)

Supplementary Table 2. Crystallographic data obtained from the Λ-Pcage.

Empirical formula	$C_{60.5}H_{63}N_6OP_2$
Formula weight	952.11
Temperature/K	173.00
Crystal system	monoclinic
Space group	C2
a/Å	19.9776(6)
b/Å	23.2865(6)
c/Å	26.0454(7)
α/°	90
β/°	97.9710(10)
γ/°	90
Volume/Å^3	11999.5(6)
Z	8
ρ_{calc}g/cm^3	1.054
μ/mm^{-1}	0.631
F(000)	4048.0
Crystal size/mm^3	0.41 × 0.39 × 0.36
Radiation	GaKα (λ = 1.34139)
2θ range for data collection/°	6.174 to 109.000
Index ranges	$-24 \leq h \leq 22$, $-28 \leq k \leq 28$, $-31 \leq l \leq 31$
Reflections collected	80296
Independent reflections	22244 [R_{int} = 0.0254]
Data/restraints/parameters	22244/33/1271
Goodness-of-fit on F^2	1.042
Final R indexes [$I \geq 2\sigma$ (I)]	R_1 = 0.0347, wR_2 = 0.0976
Final R indexes [all data]	R_1 = 0.0355, wR_2 = 0.0983
Largest diff. peak/hole/e Å^{-3}	0.88/-0.26
Flack parameter	0.062(3)

Supplementary Table 3. Crystallographic parameters and atomic coordinates for Δ-P-COF-1 model arranged in different stacking modes.

Stacking mode	A-A (eclipsed)	
Space group	*P*3	
Crystal system	hexagonal	
Unit cell parameters	*a* = 34.3878 Å	α = 90°
	b = 34.3878 Å	β = 90°
	c = 3.4773Å	γ= 120°
Stacking mode	A-B (staggered)	
Space group	*P*3	
Crystal system	hexagonal	
Unit cell parameters	*a* = 34.399 Å	α = 90°
	b = 34.399 Å	β = 90°
	c = 6.5323 Å	γ= 120°
Stacking mode	A-B-C (staggered-interpenetrated)	
Space group	*R*-3	
Crystal system	trigonal	
Unit cell parameters	*a* = 34.3878 Å	α = 90°
	b = 34.3878 Å	β = 90°
	c = 10.4319 Å	γ= 120°

Supplementary Table 4. Crystallographic parameters and atomic coordinates for Δ-P-COF-2 model arranged in different stacking modes.

Stacking mode	A-A (eclipsed)	
Space group	*P*3	
Crystal system	hexagonal	
Unit cell parameters	*a* = 34.2982 Å	α = 90°
	b = 34.2982 Å	β = 90°
	c = 3.4634 Å	γ= 120°
Stacking mode	A-B (staggered)	
Space group	*P*3	
Crystal system	hexagonal	
Unit cell parameters	*a* = 34.3031 Å	α = 90°
	b = 34.3013 Å	β = 90°
	c = 6.5065 Å	γ= 120°
Stacking mode	A-B-C (staggered-interpenetrated)	
Space group	*R*-3	
Crystal system	trigonal	
Unit cell parameters	*a* = 34.2982 Å	α = 90°
	b =34.2982 Å	β = 90°
	c = 10.3901 Å	γ= 120°

Supplementary Table 5. Crystallographic parameters and atomic coordinates for Δ-P-COF-3 model arranged in different stacking modes.

Stacking mode	A-A (eclipsed)	
Space group	*P*6	
Crystal system	hexagonal	
Unit cell parameters	*a* = 39.0794 Å	α = 90°
	b = 39.0794 Å	β = 90°
	c = 5.6807 Å	γ= 120°
Stacking mode	A-B (staggered)	
Space group	*P*63	
Crystal system	hexagonal	
Unit cell parameters	*a* = 39.0851 Å	α = 90°
	b = 39.0851 Å	β = 90°
	c = 10.9338 Å	γ= 120°
Stacking mode	A-B-C (staggered-interpenetrated)	
Space group	*R*-3	
Crystal system	trigonal	
Unit cell parameters	*a* = 39.0344Å	α = 90°
	b = 39.0344 Å	β = 90°
	c = 14.7963 Å	γ= 120°

Supplementary Table 6. The summary of different piezoelectric parameters of chiral P-COF series and achiral P-COF counterpart measured by PFM and KPFM.

	chiral P-COF-1		chiral P-COF-2		chiral P-COF-3		achiral AP-COF-3
	Δ-	Λ-	Δ-	Λ-	Δ-	Λ-	
PFM amplitude (pm)	195	204	350	341	1150	1240	~150
PFM phase (°)	177.4	180.1	170.5	179.6	179.8	182.5	~146
PFM measured d_{33} (pm/V)	35.8	37.7	61.9	68.5	159.4	171.0	23.8
KPFM potential (mV)	−45.2	−48.9	−92.1	−77.3	−240.5	−272.8	−19.1

Supplementary Table 7. The comparison of piezoelectric parameters of different types of piezoelectric materials.

Category	Structure	d_{33} (pC/N)	g_{33} (×10^{-3}	$\varepsilon_r{}^a$	V_{oc}	Ref.
Inorganic oxides	PMN-PT	2800	38.5	8200	–	(1)
	STO	93	35.0	300	–	(2)
	$LiNbO_3$	21	67.7	35	–	(3)
	$LiTaO_3$	15	37.6	45	–	(4)
	$PbTiO_3$	120	67.7	200	170	(5)
	PZT-4	280	24.3	1300	–	(6)
	PZT-8	230	26.0	1000	–	(6)
	PZT-5H	600	19.6	3450	–	(7)
	PZT-5A	350	21.9	1800	–	(7)
	KTN	416	12.5	3742	–	(8)
	BTO	190	9.4	3600	–	(9)
	Lithium tetraborate	10.1	58.5	19.5	–	(10)
	KNNS	208	61.5	532	–	(11)
	NBT-KBT	150	20.5	1150	–	(12)
Inorganic -organic hybrid perovskite	TMCM-$CdCl_3$	220	1910	13.0	–	(13)
	TMCM-$MnCl_3$	185	1681	12.4	–	(14)
	TMBM-$MnBr_3$	112	1120	11.3	–	(15)
	$(TMCM)_2$-$SnCl_6$	137	980	15.8	81	(16)
	$(ATHP)_2$-$PbBr_4$	76	660	13	–	(17)
	TMCM-$GaCl_4$	226	1318	19.3	38.1	(18)
	$MAPbI_3$	54	122	50	–	(19)
	TMCM-$CdBrCl_2$	440	6215	8	–	(20)
	$C_6H_5N(CH_3)_3$ $CdBr_2Cl_{0.75}$	367	3595	11.5	210	(21)
Organic Small molecules	$[AH][ReO_4]$	90	338	30	–	(22)
	Triglycine sulfate	22	37.1	67	–	(23)
	DPDP·ClO_4	12	149.2	9.1	–	(24)

	TPAP·BF_4	3	36.5	9.3	7.37	(24)
	TIAP·BF_4	3	20.3	16.7	4.75	(24)
	Rochelle salt	7	85.9	9.2	0.03	(25)
	HFPD	138	2450	6.4	18	(26)
	DPFO	120	2708	5.0	–	(27)
	Spirooxazac-amphorsult-am	10	250.8	45	–	(28)
Bio-molecules	γ-glycine	10	451.5	2.5	0.45	(29)
	FF dipeptide	17.9	505.1	4.0	1.4	(30)
	collagen	5	112.9	5.0	–	(31)
	cellulose nanofiber	5.7	185.4	3.5	–	(32)
	β-chitin	4	112.9	4.0	1.0	(33)
	lysozyme	6.5	1.3	43.2	0.008	(34)
	virus	1.9	–	–	–	(35)
Polymers	PVDF	28	263.5	12.0	12	(36)
	P(VDF-TrFE)	38	357.7	12.0	20	(37)
	BOPVDF	62	359.0	19.5	–	(38)
	Glycine-PCL	19	476.5	4.5	–	(39)
	PVDF fiber	17	114.9	16.7	48	(40)
	PVDF-PANI	32	328.3	11.0	10	(41)
	PHB/CNT	15.1	426.4	4.0	12	(42)
Molecular cages	RCC1-Cl	3.5	131	3.0	4.1	(43)
	RCC3-SO_4	3.3	124	3.0	5.4	(43)
	MOC-FA3	2.2	170	1.5	–	(44)
MOFs	MIL-125	1.7	295	0.9	–	(45)
	NH_2-MIL-125	11.8	205	0.9	–	(45)
	Cu-NH_2-MIL-12	26.2	350	11.8	–	(45)
	UiO66-NH_2(Zr)	4	60	10.5	–	(46)
	UiO66-NH_2(Hf)	139	1800	12.1	–	(46)
	Zn-Car MOF	11.2	156	11.3	40	(47)
	IISERP-MOF2	21.3	859.4	3.9	13	(48)

COFs	TP-BT-0F-COF	5.5	310.4	2.0	–	(49)
	BTA-BT-0F-COF	5.1	230.2	2.5	–	(49)
	TP-BT-1F-COF	4.7	176.8	3.0	–	(49)
	TP-BT-2F-COF	4.1	178.0	2.6	–	(49)
	CityU-13	20.9	907.3	2.6	60	(50)
	CityU-14	18.9	853.3	2.5	50	(50)
	chiral Δ-P-COF-1	29.9	1540	2.2	8	This work
	chiral Λ-P-COF-1	29.9	1540	2.2	9	
	chiral Δ-P-COF-2	57.1	2710	2.4	31	
	chiral Λ-P-COF-2	57.5	2705	2.4	29	
	chiral Δ-P-COF-3	186.8	7640	2.7	75	
	chiral Λ-P-COF-3	184.8	7560	2.7	74	
	achiral AP-COF-3	12.1	495	2.7	12	

[a]The piezoelectric voltage coefficient g_{33} is calculated from the d_{33} and permittivity (ε_{33}) of different materials based on the equation of $g_{33} = d_{33}/\varepsilon_{33}\varepsilon_0$, where ε_0 is the permittivity of vacuum (8.854×10^{-12} F/m), ε_{33} is equal to ε_r obtained from quasi-static measurement.

Supplementary Table 8. The elastic properties of chiral P-COF series.

	Young's moduli		Anisotropy	Shear moduli (GPa)		Anisotropy
	E_{max}	E_{min}		E_{max}	E_{min}	
Δ-P-COF-	28.1	18.6	1.5	9.8	7.9	1.2
Δ-P-COF-	30.9	13.7	2.3	15.2	6.9	2.2
Δ-P-COF-	32.6	7.5	4.3	18.6	3.1	6.0

Supplementary Table 9. The matrix calculation of piezoelectric strain constant (d_{ij}) of chiral P-COF series.

For Δ-P-COF-1,

(1) The elastic stiffness constant (C_{ij}) is as following,

$$C_{ij} = \begin{bmatrix} 20.2 & 3.5 & 9.5 & 0.022 & 0.045 & 0 \\ 3.5 & 20.2 & 9.5 & -0.022 & -0.045 & 0 \\ 9.5 & 9.5 & 38.7 & 0 & 0 & 0 \\ 0.022 & -0.022 & 0 & 8.1 & 0 & -0.045 \\ 0.045 & -0.045 & 0 & 0 & 8.1 & 0.022 \\ 0 & 0 & 0 & -0.045 & 0.022 & 8.4 \end{bmatrix}$$

(2) The piezoelectric stress constant (e_{ij}) is obtained from DFT,

$$e_{ij} = \begin{bmatrix} 0.113 & -0.113 & 0 & 0.0163 & -0.0784 & 0.0974 \\ 0.0974 & -0.0974 & 0 & -0.0752 & -0.00392 & -0.113 \\ -0.0318 & -0.0318 & 0.874 & 0 & 0 & 0 \end{bmatrix}$$

(3) The piezoelectric strain constant (d_{ij}) is as below,

$$d_{ij} = e_{ij} \times s_{ij} = e_{ij} \times C_{ij}^{-1} = \begin{bmatrix} 6.8 & -6.8 & 0 & 2.0 & -9.8 & 11.7 \\ 5.8 & -5.8 & 0 & -9.4 & -0.5 & -13.5 \\ -13.0 & -13.0 & 29.1 & 0 & 0 & 0 \end{bmatrix}$$

For Δ-P-COF-2,

(1) The elastic stiffness constant (C_{ij}) is as following,

$$C_{ij} = \begin{bmatrix} 33.5 & 2.8 & 18.0 & 0.30 & 0.41 & 0 \\ 2.8 & 33.5 & 18.0 & -0.30 & -0.41 & 0 \\ 18.0 & 18.0 & 28.6 & 0 & 0 & 0 \\ 0.30 & -0.30 & 0 & 13.5 & 0 & -0.41 \\ 0.41 & -0.41 & 0 & 0 & 13.5 & 0.30 \\ 0 & 0 & 0 & -0.41 & 0.30 & 15.4 \end{bmatrix}$$

(2) The piezoelectric stress constant (e_{ij}) is obtained from DFT,

$$e_{ij} = \begin{bmatrix} 0.312 & -0.312 & 0 & 0.0336 & -0.124 & 0.109 \\ 0.109 & -0.109 & 0 & -0.121 & -0.0166 & -0.0928 \\ -0.0994 & -0.0994 & 0.669 & 0 & 0 & 0 \end{bmatrix}$$

(3) The piezoelectric strain constant (d_{ij}) is as below,

$$d_{ij} = e_{ij} \times s_{ij} = e_{ij} \times C_{ij}^{-1} = \begin{bmatrix} 10.3 & -10.3 & 0 & 2.3 & -10.0 & 7.4 \\ 3.7 & -3.7 & 0 & -9.3 & -1.3 & -6.3 \\ -38.6 & -38.6 & 72.1 & 0 & 0 & 0 \end{bmatrix}$$

For Δ-P-COF-3,

(1) The elastic stiffness constant (C_{ij}) is as following,

$$C_{ij} = \begin{bmatrix} 37.3 & -0.87 & 14.7 & 0 & 0 & 0 \\ -0.87 & 37.3 & 14.7 & 0 & 0 & 0 \\ 14.7 & 14.7 & 17.5 & 0 & 0 & 0 \\ 0 & 0 & 0 & 11.9 & 0 & 0 \\ 0 & 0 & 0 & 0 & 11.9 & 0 \\ 0 & 0 & 0 & 0 & 0 & 19.1 \end{bmatrix}$$

(2) The piezoelectric stress constant (e_{ij}) is obtained from DFT,

$$e_{ij} = \begin{bmatrix} 0 & 0 & 0 & 0.0201 & -0.156 & 0 \\ 0.0156 & -0.0156 & 0 & -0.0201 & 0 & 0 \\ 0.0904 & 0.0904 & 0.740 & 0 & 0 & 0 \end{bmatrix}$$

(3) The piezoelectric strain constant (d_{ij}) is as below,

$$d_{ij} = e_{ij} \times s_{ij} = e_{ij} \times C_{ij}^{-1} = \begin{bmatrix} 0 & 0 & 0 & 1.7 & -13.1 & 0 \\ 4.1 & -4.1 & 0 & -1.7 & 0 & 0 \\ -82.3 & -82.3 & 212.2 & 0 & 0 & 0 \end{bmatrix}$$

Supplementary Table 10. The performance contrast of different types of piezoelectric composite devices in key parameters.

	V_{oc} (V)	I_{sc} (μA)	S (mV/kPa)	Linear sensing range (kPa)	Ref.
BCZT-NF@BCZT-SP@Ag fibers	96.4	4.86	2970	25–75	(51)
Cu-Fe-PVDF	8	3	20	7–270	(52)
P(VDF-TrFE)/PA	5.6	−	35	24–160	(53)
MXene/PVDF	28	1.71	840	8.3–33.3	(54)
BeO-B8/PVDF	8	2.5	430	0–18.6	(55)
PVDF/PDMS	9	1.6	7.2	0–6	(56)
$BaTiO_3$/PDMS	60	0.6	472	0–100	(57)
PEG/SIS	1.01	−	135	1.5–7.5	(58)
P(VDF-TrFE)/CNTs @Al_2O_3	36.5	0.84	527	0.1–80	(59)
CD/BT-OH/MXene	7	−	320	0–125	(60)
ZnO/PDVF	3.5	0.35	330	1–30	(61)
PZT/PDMS	1.25	−	8.59	1.25–250	(62)
AgNWs@PTFE/ Graphene/PVDF	1.52	−	92	0–100	(63)
Δ-P-COF-1	8	1.7	873	0–32	This work
Δ-P-COF-2	31	4.9	2150	0–32	
Δ-P-COF-3	75	9.0	4710	0–32	

Reference

(1) Zhang, S., Li, F., Jiang, X., Kim, J., Luo, J. & Geng, X. Advantages and challenges of relaxor-$PbTiO_3$ ferroelectric crystals for electroacoustic transducers—A review. *Prog. Mater. Sci.* **68**, 1-66 (2015).

(2) Anderson, C. P., Scuri, G., Chan, A., Eun, S., White, A. D., Ahn, G. H., Jilly, C., Safavi-Naeini, A., van Gasse, K., Li, L. & Vučković, J. Quantum critical electro-optic and piezo-electric nonlinearities. *Science* **390**, 394-399 (2025).

(3) Smith, R. T. & Welsh, F. S. Temperature dependence of the elastic, piezoelectric, and dielectric constants of lithium tantalate and lithium niobate. *J. Appl. Phys.* **42**, 2219-2230 (1971).

(4) Hamze, A. K., Reynaud, M., Geler-Kremer, J. & Demkov, A. A. Design rules for strong electro-optic materials. *npj Comput. Mater.* **6**, 130 (2020).

(5) Jian, G., Jiao, Y., Meng, Q., Guo, Y., Wang, F., Zhang, J., Wang, C., Moon, K.-S. & Wong, C.-P. Excellent high-temperature piezoelectric energy harvesting properties in flexible polyimide/3D $PbTiO_3$ flower composites. *Nano Energy* **82**, 105778 (2021).

(6) Haertling, G. H. Ferroelectric ceramics: History and technology. *J. Am. Ceram. Soc.* **82**, 797-818 (1999).

(7) Liu, Z., Wu, H., Ren, W. & Ye, Z.-G. Piezoelectric and ferroelectric materials: Fundamentals, recent progress, and applications. *3rd ed. Elsevier Inc.* 135-171 (2023).

(8) Tian, H., Meng, X., Hu, C., Tan, P., Cao, X., Shi, G., Zhou, Z. & Zhang, R. Origin of giant piezoelectric effect in lead-free $K_{1-x}Na_xTa_{1-y}Nb_yO_3$ single crystals. *Sci. Rep.* **6**, 25637 (2016).

(9) Zgonik, M., Bernasconi, P., Duelli, M., Schlesser, R., Günter, P., Garrett, M. H., Rytz, D., Zhu, Y. & Wu, X. Dielectric, elastic, piezoelectric, electro-optic, and elasto-optic tensors of $BaTiO_3$ crystals. *Phys. Rev. B* **50**, 5941-5949 (1994).

(10) Zhang, S. & Yu, F. Piezoelectric materials for high temperature sensors. *J. Am. Ceram. Soc.* **94**, 3153-3170 (2011).

(11) Chang, Y., Poterala, S. F., Yang, Z., Trolier-McKinstry, S. & Messing, G. L. 001

textured $(K_{0.5}Na_{0.5})(Nb_{0.97}Sb_{0.03})O_3$ piezoelectric ceramics with high electromechanical coupling over a broad temperature range. *Appl. Phys. Lett.* **95**, 232905 (2009).

(12) Zhao, S., Li, G., Ding, A., Wang, T. & Yin, Q. Ferroelectric and piezoelectric properties of $(Na, K)_{0.5}Bi_{0.5}TiO_3$ lead free ceramics. *Phys. D: Appl. Phys.* **39**, 2277 (2006).

(13) Song, X.-J., Xiong, Y.-A., Zhou, R.-J., Cao, X.-X., Jing, Z.-Y., Ji, H.-R., Gu, Z.-X., Sha, T.-T., Xiong, R.-G. & You, Y.-M. The first demonstration of strain-controlled periodic ferroelectric domains with superior piezoelectric response in molecular materials. *Adv. Mater.* **35**, 2211584 (2023).

(14) You, Y.-M., Liao, W.-Q., Zhao, D., Ye, H.-Y., Zhang, Y., Zhou, Q., Niu, X., Wang, J., Li, P.-F., Fu, D.-W., Wang, Z., Gao, S., Yang, K., Liu, J.-M., Li, J., Yan, Y. & Xiong, R.-G. An organic-inorganic perovskite ferroelectric with large piezoelectric response. *Science* **357**, 306-309 (2017).

(15) Liao, W.-Q., Tang, Y.-Y., Li, P.-F., You, Y.-M. & Xiong, R.-G. Large piezoelectric effect in a lead-free molecular ferroelectric thin film. *J. Am. Chem. Soc.* **139**, 18071-18077 (2017).

(16) Huang, G., Khan, A. A., Rana, M. M., Xu, C., Xu, S., Saritas, R., Zhang, S., Abdel-Rahmand, E., Turban, P., Ababou-Girard, S., Wang, C. & Ban, D. Achieving ultrahigh piezoelectricity in organic–inorganic vacancy-ordered halide double perovskites for mechanical energy harvesting. *ACS Energy Lett.* **6**, 16-23 (2021).

(17) Chen, X.-G., Song, X.-J., Zhang, Z.-X., Li, P.-F., Ge, J.-Z., Tang, Y.-Y., Gao, J.-X., Zhang, W., Fu, D., You, Y.-M. & Xiong, R.-G. Two-dimensional layered perovskite ferroelectric with giant piezoelectric voltage coefficient. *J. Am. Chem. Soc.* **142**, 1077-1082 (2020).

(18) Wang, B., Hong, J., Yang, Y., Zhao, H., Long, L. & Zheng, L. Achievement of a giant piezoelectric coefficient and piezoelectric voltage coefficient through plastic molecular-based ferroelectric materials. *Matter* **5**, 1296-1304 (2022).

(19) Garten, L. M., Moore, D. T., Nanayakkara, S. U., Dwaraknath, S., Schulz, P., Wands, J., Rockett, A., Newell, B., Persson, K. A., Trolier-McKinstry, S. & Ginley,

D. S. The existence and impact of persistent ferroelectric domains in $MAPbI_3$. *Sci. Adv.* **5**, eaas9311 (2019).

(20) Chen, X.-G., Tang, Y.-Y., Lv, H.-P., Song, X.-J., Peng, H., Yu, H., Liao, W.-Q., You, Y.-M., Xiong, R.-G. Remarkable enhancement of piezoelectric performance by heavy halogen substitution in hybrid perovskite ferroelectrics. *J. Am. Chem. Soc.* **145**, 1936-1944 (2023).

(21) Hu, Y., Parida, K., Zhang, H., Wang, X., Li, Y., Zhou, X., Morris, S. A., Liew, W. H., Wang, H., Li, T., Jiang, F., Yang, M., Alexe, M., Du, Z., Gan, C. L., Yao, K., Xu, B., Lee, P. S. & Fan, H. Bond engineering of molecular ferroelectrics renders soft and high-performance piezoelectric energy harvesting materials. *Nat. Commun.* **13**, 5607 (2022).

(22) Harada J, Kawamura Y, Takahashi Y, Uemura Y, Hasegawa T, Taniguchi H, Maruyama K. Plastic/ferroelectric crystals with easily switchable polarization: Low-voltage operation, unprecedentedly high pyroelectric performance, and large piezoelectric effect in polycrystalline forms. *J. Am. Chem. Soc.* **141**, 9349-9357 (2019).

(23) Senthil Pandian, M., Verma, S., Ramasamy, P., Singh, G., Gupta, S. M., Tiwari, V. S. & Karnal, A. K. Growth of [010] oriented urea-doped triglycine sulphate (Ur-TGS) single crystals below and above Curie temperature (Tc) and comparative investigations of their physical properties. *Appl. Phys. A* **126**, 492 (2020).

(24) Vijayakanth, T., Ram, F., Praveenkumar, B., Shanmuganathan, K. & Boomishankar, R. All-organic composites of ferro- and piezoelectric phosphonium salts for mechanical energy harvesting application. *Chem. Mater.* **31**, 5964-5972 (2019).

(25) Lemaire, E., Moser, R., Borsa, C. J. & Briand, D. Green paper-based piezoelectronics for sensors and actuators. *Sensor. Actuat. A-Phys.* **244**, 285-291 (2016).

(26) Zhang, H.-Y., Tang, Y.-Y., Gu, Z.-X., Wang, P., Chen, X.-G., Lv, H.-P., Li, P.-F., Jiang, Q., Gu, N., Ren, S. & Xiong, R.-G. Biodegradable ferroelectric molecular crystal with large piezoelectric response. *Science* **383**, 1492-1498 (2024).

(27) Ivanov, M., Nikitin, T., Lopes, S., Duan, Y., Xu, J., Fausto, R., Paixão, J. A.,

Vilarinho, P. M., Rasing, T. & Semin, S. Thickness-dependent high-temperature piezo- and ferro-electricity in a fluorenone-based molecular crystal. *Adv. Mater. Interfaces* **9**, 2201103 (2022).

(28) Song, X.-J., Tang, S.-Y., Chen, X.-G. & Ai, Y. Chemical design of homochiral heterocyclic organic ferroelectric crystals. *Chem. Commun.* **58**, 10361-10364 (2022).

(29) Guerin, S., Stapleton, A., Chovan, D., Mouras, R., Gleeson, M., McKeown, C., Noor, M. R., Silien, C., Rhen, F. M. F., Kholkin A. L., Liu, N., Soulimane, T., Tofail, S. A. M. & Thompson, D. Control of piezoelectricity in amino acids by supramolecular packing. *Nat. Mater.* **17**, 180-186 (2018).

(30) Nguyen, V., Zhu, R., Jenkins, K. & Yang, R. Self-assembly of diphenylalanine peptide with controlled polarization for power generation. *Nat. Commun.* **7**, 13566 (2016).

(31) Cartwright, V. F. & Brown, C. P. Hierarchical piezoresponse in collagen. *Adv. Mater. Technol.* **7**, 2101166 (2022).

(32) Rajala, S., Siponkoski, T., Sarlin, E., Mettänen, M., Vuoriluoto, M., Pammo, A., Juuti, J., Rojas, O. J., Franssila, S. & Tuukkanen, S. Cellulose nanofibril film as a piezoelectric sensor material. *ACS Appl. Mater. Interfaces* **8**, 15607-15614 (2016).

(33) Kim, K., Ha, M., Choi, B., Joo, S. H., Kang, H. S., Park, J. H., Gu, B., Park, C., Park, C., Kim, J., Kwak, S. K., Ko, H., Jin, J. & Kang, S. J. Biodegradable, electro-active chitin nanofiber films for flexible piezoelectric transducers. *Nano Energy* **48**, 275-283 (2018).

(34) Stapleton, A., Noor, M. R., Sweeney, J., Casey, V., Kholkin, A. L., Silien, C., Gandhi, A. A., Soulimane, T. & Tofail, S. A. M. The direct piezoelectric effect in the globular protein lysozyme. *Appl. Phys. Lett.* **111**, 142902 (2017).

(35) Lee, B. Y., Zhang, J. X., Zueger, C., Chung, W.-J., Yoo, S. Y., Wang, E., Meyer, J., Ramesh, R. & Lee, S.-W. Virus-based piezoelectric energy generation. *Nat. Nanotechnol.* **7**, 351–356 (2012).

(36) Foster, F. S., Harasiewicz, K. A. & Sherar, M. D. A history of medical and biological imaging with polyvinylidene fluoride (PVDF) transducers. *IEEE Trans*

Ultrason Ferroelectr Freq Control. **47**, 1363-1371 (2000).

(37) Sun, Q., Xia, W., Liu, Y., Ren, P., Tian, X. & Hu, T. The dependence of acoustic emission performance on the crystal structures, dielectric, ferroelectric, and piezoelectric properties of the P(VDF-TrFE) sensors. *IEEE Trans Ultrason Ferroelectr Freq Control.* **67**, 975-983 (2020).

(38) Huang, Y., Rui, G., Li, Q., Allahyarov, E., Li, R., Fukuto, M., Zhong, G.-J., Xu, J.-Z., Li, Z.-M,, Taylor, P. L. & Zhu, L. Enhanced piezoelectricity from highly polarizable oriented amorphous fractions in biaxially oriented poly(vinylidene fluoride) with pure β crystals. *Nat. Commun.* **12**, 675 (2021).

(39) Chorsi, M. T., Le, T. T., Lin, F., Vinikoor, T., Das, R., Stevens, J. F., Mundrane, C., Park, J., Tran, K. T. M., Liu, Y., Pfund, J., Thompson, R., He, W., Jain, M., Morales-Acosta, M. D., Bilal, O. R., Kazerounian, K., Ilies, H. & Nguyen, T. D. Highly piezoelectric, biodegradable, and flexible amino acid nanofibers for medical applications. *Sci. Adv.* **9**, eadg6075 (2023).

(40) Tiwari, S., Gaur, A., Kumar, C. & Maiti, P. Ionic liquid-based electrospun polymer nanohybrid for energy harvesting. *ACS Appl. Electron. Mater.* **3**, 2738-2747 (2021).

(41) Maity, K., Garain, S., Henkel, K., Schmeißer, D. & Mandal, D. Self-powered human-health monitoring through aligned PVDF nanofibers interfaced skin-interactive piezoelectric sensor. *ACS Appl. Polym. Mater.* **2**, 862-878 (2020).

(42) Cai, Z., Xiong, P., He, S. & Zhu, C. Improved piezoelectric performances of highly orientated poly(β-hydroxybutyrate) electrospun nanofiber membrane scaffold blended with multiwalled carbon nanotubes. *Mater. Lett.* **240**, 213-216 (2019).

(43) Ye, Y.-Z., Liu, H.-Y., Gong, Y.-J., Xu, Z.-Z, Zhao, Y., Yu, N., Wang, Q.-S., Wen, W., Yang, T.-Y, Li, W. & Jiang, S. Design of piezoelectric organic cage salts for energy harvesting. *Chem* **10**, 1118-1131 (2024).

(44) Li, X.-A., Wang, Y., Liang, Z.-Z., Peng, X.-B., Xiao, L.-M., Gong, L., Yang, X., Zou, B., Zhou, Y. & Liu, J.-M. A dual-piezoelectric metal–organic cage/COF Z-scheme heterojunction for solar-mechanical water splitting. *Adv. Sci.* **13**, e23030 (2026).

(45) Hu, H., Li, X., Zhang, K., Yan, G., Kong, W., Qin, A., Ma, Y., Li, A., Wang, K.,

Huang, H., Sun, X. & Ma, T. Dual modification of metal-organic frameworks for exceptional high piezo-photocatalytic hydrogen production. *Adv. Mater.* **37**, 2419023 (2025).

(46) Zhang, C., Lei, D., Xie, C., Hang, X., He, C. & Jiang, H.-L. Piezo-photocatalysis over metal-organic frameworks: Promoting photocatalytic activity by piezoelectric effect. *Adv. Mater.* **33**, 2106308 (2021).

(47) Wang, Y., Su, P., Lin, Z., Li, X., Chen, K., Ye, T., Li, Y., Zou, Y. & Wang, W. A tribo/piezoelectric nanogenerator based on bio-MOFs for energy harvesting and antibacterial wearable device. *Adv. Mater.* **37**, 2418207 (2025).

(48) Yang, T.-Y., Li, Z.-G., Lang, F., Dong, X.-H., Zhao, C., Zhang, G.-L., Li, Z.-Y., Chang, Z., Feng, R., Li, W. & Bu, X.-H. Large piezoelectricity in a dynamic metal-organic framework with negative linear compressibility. *J. Am. Chem. Soc*. **147**, 41988-41994 (2025).

(49) Liang, Z.-Z., Wang, Y., Li, X.-A., Peng, X.-B., Gong, L., Xiao, L.-M,, Yang, X., Zou, B., Zhou, Y. & Liu, J.-M. Enhanced piezo-photocatalytic water splitting activity via engineering robust dipole moments in covalent organic frameworks. *Nat. Commun.* **17**, 729 (2025).

(50) Gu, Q., Lu, X., Chen, C., Wang, X., Kang, F., Li, Y. Y., Xu, Q., Lu, J., Han, Y., Qin, W. & Zhang, Q. C. High-performance piezoelectric two-dimensional covalent organic frameworks. *Angew. Chem. Int. Ed.* **63**, e202409708 (2024).

(51) Lu, H., Hu, Z., Wang, X., Chen, G., Zheng, X., Xia, J., Huang, M., Yang, W., Liu, J. & Hu, B. Performance enhancement of nanogenerator achieved in branch-heterostructure piezoelectric ceramic fiber toward electrical transmission power line monitoring. *J. Adv. Ceram.* **14**, 9221171 (2025).

(52) Haldar, R., Sarkar, U., Kumar, A., Mandal, D. & Shanmugam, M. Inducing Polar Phase in Poly(vinylidene fluoride) with a molecular ferroelectric copper(II) complex for piezoelectric energy harvesting. *Adv. Funct. Mater.* **34**, 2407611 (2024).

(53) Zhao, T., Li, Z., Li, Y., Chai, B., Xie, W., Gao, B., Xue, K., Huang, X., Ye, X., Fan, C. & Zhang, Z. High sensitivity, all-organic piezoelectric skin enabled by a phytic acid-assisted molecular engineering strategy. *ACS Nano* **20**, 1628-1638 (2026).

(54) Jadhav, S., Pham, H. D., Padwal, C., Chougale, M., Brown, C., Motta, N., Ostrikov, K., Bae, J. & Dubal, D. Enhancing mechanical energy transfer of piezoelectric supercapacitors. *Adv. Mater. Technol.* **7**, 2100550 (2022).

(55) Patil, C. S., Kim, J., Ghode, S. B., Paranjape, M. V., Sawant, J. K., Noman, M., Saqib, Q. M., Kim, M. H., Sung, S. H., Gore, A. H., Kurkuri, M. D., Jeon, Y. P. & Bae, J. High Flexible, Ultra-robust piezoelectric nanogenerator based on hexagonal α-beryllium oxide/ PVDF composite thin film: E-skin and energy harvesting applications. *Adv. Funct. Mater.* **36**, e17516 (2026).

(56) Lin, W., Wang, B., Peng, G., Shan, Y., Hu, H. & Yang, Z. Skin-inspired piezoelectric tactile sensor array with crosstalk-free row+column electrodes for spatiotemporally distinguishing diverse stimuli. *Adv. Sci.* **8**, 2002817 (2021).

(57) Wei, X., Xu, K., Wang, Y., Zhang, Z. & Chen, Z. 3D Printing of flexible $BaTiO_3$/polydimethylsiloxane piezocomposite with aligned particles for enhanced energy harvesting. *ACS Appl. Mater. Interfaces* **16**, 11740-11748 (2024).

(58) Zhang, Y., Hu, X., Yan, Z., Zhang, S., Zhao, J., Sun, H., Liu, S. & Qin, Y. Ultra-soft organic combined film with piezoelectricity induced by liquid-liquid interface polar engineering. *Nat. Commun.* **16**, 6410 (2025).

(59) Zhao, H., Chen, X., Xin, C., Zhao, F., Cheng, S., Lei, M., Wang, C., Zhang, J., Chen, X., Tian, H., Zhang, J. & Shao, J. High-sensitivity and self-powered flexible pressure sensor based on multi-scale structured piezoelectric composite. *Chem. Eng. J.* **519**, 164787 (2025).

(60) Fu, Y., Li, C., Cheng, Y., He, Y., Zhang, W., Wei, Q. & Li, D. Biomass aerogel composite containing $BaTiO_3$ nanoparticles and MXene for highly sensitive self-powered sensor and photothermal antibacterial applications. *Compos. Part. A-Appl. S.* **173**, 107663 (2023).

(61) Deng, W., Yang, T., Jin, L., Yan, C., Huang, H., Chu, X., Wang, Z., Xiong, D., Tian, G., Gao, Y., Zhang, H. & Yang W. Cowpea-structured PVDF/ZnO nanofibers based flexible self-powered piezoelectric bending motion sensor towards remote control of gestures. *Nano Energy* **55**, 516-525 (2019).

(62) Hou, X., Zhang, S., Yu, J., Cui, M., He, J., Li, L., Wang, X. & Chou, X. Flexible

piezoelectric nanofibers/polydimethylsiloxane-based pressure sensor for self-powered human motion monitoring. *Energy Technol.* **8**, 1901242 (2020).

(63) Ma, M., Zhang, Z., Zhao, Z., Liao, Q., Kang, Z., Gao, F., Zhao, X. & Zhang. Y. Self-powered flexible antibacterial tactile sensor based on triboelectric-piezoelectric-pyroelectric multi-effect coupling mechanism. *Nano Energy* **66**, 104105 (2019).